Tunnelling and Underground Space Technology 153 (2024) 106001

Contents lists available at ScienceDirect

Tunnelling and Underground Space Technology incorporating Trenchless Technology Research

journal homepage: www.elsevier.com/locate/tust

A strain applied method for FEM-2D modelling of TBM tunnels in coarse-grained soils with comparative analysis of case histories

F. Schiena [a], E. Lusini [b,*], A. Lembo Fazio [a], A. Graziani [a]

[a] Department of Civil, Computer Science and Aeronautical Technologies Engineering - DICITA, Università degli Studi "Roma Tre", Via Vito Volterra 62, 00146 Roma, Italy

[b] Department of Chemical Engineering Materials Environment – DICMA, Sapienza University of Rome, via Eudossiana 18, 00183 Rome, Italy

ARTICLE INFO

Keywords:
TBM mechanized excavation
Shallow tunnels
Settlements
2D finite element analysis
Coarse-grained soils
Prescribed strains

ABSTRACT

The paper focuses on the prediction of tunnelling-induced settlements in greenfield conditions. The main components of ground deformation are investigated with approaches based on both empirical and numerical solutions. In particular, the study analyses five well documented case histories of shield-driven tunnels bored in coarse-grained soil deposits and compares the predicted and measured settlements.

A specific approach for FEM-2D modelling of soil-shield interaction (called "*Strain Applied Method*") has been implemented and its potential for the prediction of the settlement trough has been discussed. The analyses were performed for the *green field* conditions with the Finite Element software Plaxis. The mechanical behaviour of the soil has been modelled by both the usual linear elasto-plastic model (*Mohr-Coulomb, MC*) and the advanced *Hardening Soil* model with small strain stiffness (*HSs*). The comparison of results shows that the settlements calculated by the *HSs* model are generally in better agreement with the field measurements. Then, the analysis has been focused on the volume loss obtained for the five case histories, finding some significant correlations between volume loss and the specific parameters required by the proposed FEM-2D model. The predictive capabilities of the 2D model, with parameters estimated by specific correlations, were demonstrated by applying the proposed method for two new case histories, not included in the initial set utilized to find the correlations.

1. Introduction

The boring process causes stress relief on the tunnel walls as well as on the face. Since tunnelling in urban areas usually takes place at shallow depth, easily the induced deformations spread up to the ground surface and affect the existing structures. The surface settlements are influenced by the excavation method: they can be effectively controlled by using EPB or Slurry-Shield mechanized excavation, able to apply a continuous support pressure to the tunnel face. The general criteria to select the excavation method and, more specifically, the design parameters of the TBM depend on a large number of variables: soil conditions, tunnel depth, hydraulic conditions and many other technical and economic aspects, often site-specific, discussed in various guidelines and technical papers (e.g., ITA/AITES Guidelines, 2000, Pelizza, 2002, Duhme and Lee 2021, DAUB Recommendations 2022).

Even if closed-face pressurized TBMs can effectively reduce to a minimum the deformation around the cavity and, consequently, the settlements at surface, they cannot totally prevent them, due to unavoidable effects of over-excavation. Under this term Lee et al. (1992) list three major phenomena: i) the over-excavation proper, due to the larger diameter of the cutting face with respect to the shield; ii) the conicity of the shield, tapering toward the tail; iii) the gap between the soil and the lining behind the shield, normally filled with grout under pressure. All these phenomena take place behind the face, while other additional ground losses can occur in front of the face when the ideal value of support pressure is not reached, or is lost during machine maintenance or is difficult to calibrate due to mixed face conditions (Lambrughi et al., 2012).

The basic approach to the prediction of settlements is the "semi-empirical method" introduced by Peck (1969) and subsequently refined based on data from a variety of tunnelling projects (e.g., O'Reilly and New,1982; Attewell and Woodman,1982; Mair and Taylor, 1997). The semi-empirical method, based on the assumption of a "Gaussian curve" to represent the settlement trough, represents an effective tool for the preliminary design of urban tunnels, to be complemented by numerical finite element analyses in the detailed design phase.

* Corresponding author.
E-mail address: edoardo.lusini@uniroma1.it (E. Lusini).

https://doi.org/10.1016/j.tust.2024.106001
Received 6 February 2024; Received in revised form 15 July 2024; Accepted 29 July 2024
Available online 10 August 2024

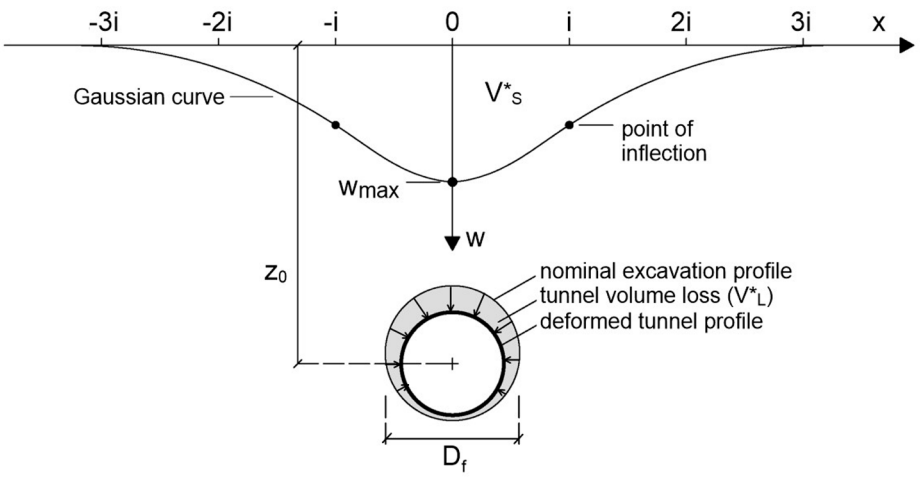

Fig. 1. Gaussian curve for transverse settlement trough, nominal tunnel diameter, volume of the settlement trough, V^*_S and volume loss at the tunnel excavation profile, V^*_L.

The Gaussian curve accurately describes the settlement trough in undrained clay but does not always match well to the trough shape in drained soils. The discrepancy increases with the intensity of yielding around the tunnel and the formation of vertical shear bands, which tend to give a chimney-like mechanism (Mair and Taylor, 1997; Celestino et al, 2000). Curves with additional degrees of freedom, such as the modified Gaussian and the yield density curves, can provide a better fit for a specific monitoring section but comparison of data from different tunnels becomes more complicated (Vorster et al., 2005; Marshall et al., 2012).

FEM modelling overcomes some limitations of the empirical methods, particularly for soil-structure interaction analyses. Two approaches of increasing complexity can be distinguished to this respect. A preliminary level modelling approach, in which tunnelling effects on existing structures are evaluated by means of uncoupled analyses: e.g., the foundation plane of the building is assumed to accommodate the greenfield displacement trough. The influence of building weight and stiffness on the settlement profile is therefore neglected. These limitations are removed in the second-level "coupled analyses", which however require the structural model of the building also being included in the global model of subsoil and tunnel (Boscardin and Cording 1989; Addenbrooke et al., 1997; Burd et al., 2000; Boldini et al., 2021; Xu et al., 2021).

FEM models have the additional advantage to make it easy to analyse the complex interaction that takes place, during the excavation advance, between soil and the support system, represented first by the TBM shield and, then, by the lining (e.g. Breth and Chambosse, 1975; Viggiani and Standing, 2001; Mair, 2003). This aspect has been investigated in full detail by 3D step-by-step modelling (Kavvadas et al. 2017; Ochmański et al., 2018). However, in engineering practice, various methods have long been developed that allow for a simpler analysis of the construction process, using 2D rather than 3D models.

It is useful to recall the main approaches utilized for 2D simplified analysis of mechanised tunnel excavation. They can be grouped into three main methods. The *Convergence-Confinement Method* (Panet and Guenot, 1983), in which the initial geostatic stress on the excavation profile is progressively reduced as a function of the face distance where the support annulus is installed. The *Gap Method* (Rowe et al., 1983) in which an initial mismatch is considered between the support annulus and the excavation profile, maintaining lining and soil unconnected until the initial gap is closed. The *Contraction Method* (Vermeer and Brinkgreve, 1993) can be considered a variation of the gap method in which the support annulus is uniformly contracted accordingly to the TBM overcut and shield diameter, and therefore forced to maintain a nearly circular shape. Finally, the *Grout Pressure Method* (Möller, 2006; Möller and Vermeer, 2008) in which the initial geostatic stress is replaced by a grout pressure distribution into an annular ring of soil elements around the tunnel lining.

While pressure-controlled methods exhibit a narrower settlement profile with respect to displacement-controlled ones, however, it has been observed that, for both approaches, the numerical analyses tend to predict settlement troughs wider than those observed experimentally, in small-scale centrifuge tests (Song and Marshall, 2020) as well as in real tunnels (Möller, 2006; Schiena, 2020).

In this paper a new procedure for modelling excavation and shield-soil interaction in 2D conditions will be presented (called "*Strain Applied Method*"). The proposed approach, suitable for implementation in FEM codes, brings together some aspects of the *Gap* and *Contraction* methods and involves a two-stage evaluation procedure of the deformations to be imposed around the tunnel section.

The imposed strains can be easily calibrated based on surface volume losses.

The performance of the method will be analysed by comparing the computed results to the measurements in greenfield conditions recorded in five well-documented case histories. The analyses were performed by two different soil models: the conventional ideal elastoplastic model with *Mohr-Coulomb (MC)* strength criterion and the *Hardening Soil* model with small strain stiffness *(Hardening)* model implemented in Plaxis 2D code (Brinkgreve et al., 2017). In fact, it has been already observed that a non-linear stiffness constitutive model can significantly improve the capabilities of FEM models, particularly for coarse-grained soils (e.g., Addenbrooke et al., 1997; Hejazi et al., 2008).

It will be shown that the settlements predicted by the developed procedure in combination with the *HSs* soil model, are generally in better agreement with field data and empirical predictions (Gaussian curves), rather than those obtained with the conventional linear elasto-plastic *MC* model. A specific section of the paper will be devoted to the influence of soil dilatancy and volumetric cap, within the *HSs* model, on the predicted settlements at ground surface.

The comparative study of the five case histories, in terms of maximum settlement and shape of the settlement trough, has led to identify a strong correlation between overall settlement parameters, particularly the surface volume loss, and the specific deformation parameters, to be imposed at the tunnel level, required by the proposed procedure. Therefore, the obtained results were employed to set up a framework of relationships useful for the assessment of the parameters required by 2D tunnel modelling in coarse-grained soil conditions. The use of such relationships has been demonstrated by their application for two new cases of tunnel excavated in Italy.

The comparative analysis has been extended also to other aspects

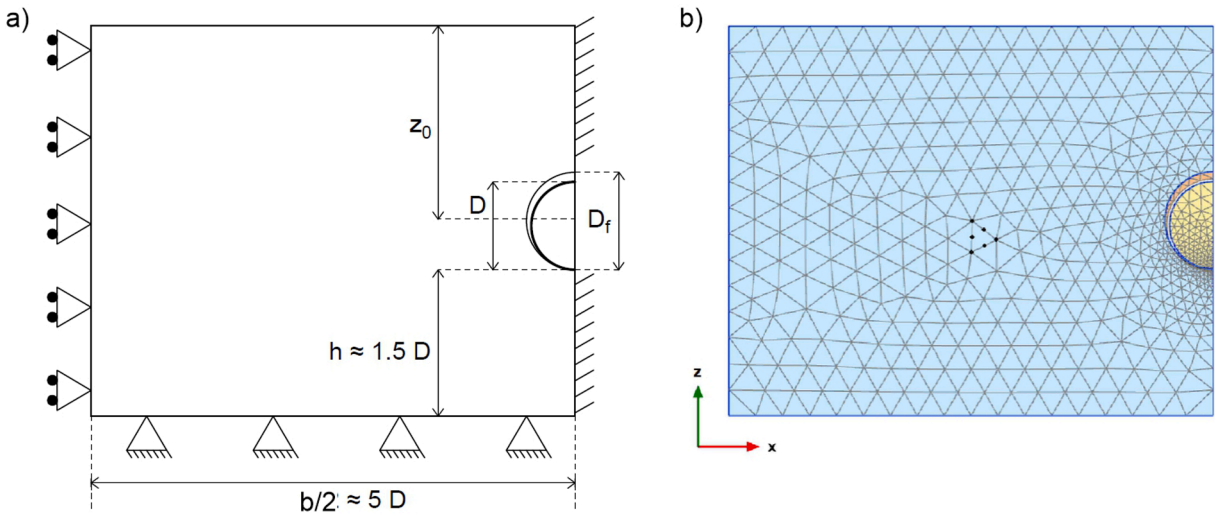

Fig. 2. Typical dimensions of the finite element model (a) and example mesh for greenfield analyses (b).

than solely the vertical settlements, as horizontal displacements of ground surface and internal forces in the lining, for the case histories for which these data were also available.

The *Strain Applied Method*, developed in this study for the specific case of closed-face tunnelling in coarse-grained soils, is believed to be applicable, with appropriate adaptations, even in different soil conditions. The special interest in coarse-grained soils was motivated by several ongoing tunnelling projects in Italy, which involve subsoil conditions with prevailing alluvial deposits or fine-coarse intermixed strata (e.g., Boldini et al., 2023). The basic features of sandy soil response to tunnel excavation have been thoroughly investigated by laboratory centrifuge tests, providing new insights into the influence of tunnel cover-to-diameter ratio, soil relative density and tunnel volume loss (Franza et al., 2019; Song and Marshall, 2020). However, the behaviour of real tunnel is more complex, due to the influence of non-homogeneous soil conditions and different TBM characteristics, in contrast with the perfectly controlled and idealized laboratory environment. Conversely, the focus of this study is on back analysis of real tunnelling projects: a set of 7 case histories is analysed, finding relevant common features, useful to calibrate the proposed *Strain Applied Method.*

2. Basic definitions and empirical background

This section briefly reviews the empirical equations commonly used for estimating soil settlements induced by tunnelling in greenfield condition, i.e. in absence of buildings and other interacting structures. The settlement trough induced by tunnel excavation, with constant depth of the tunnel axis, z_0, is well represented by a Gaussian curve: this is the basic assumptions of the "empirical" approach developed by Peck (1969) and extensively used in engineering practice. The surface settlements $w(x)$ in a transversal cross-section can be therefore calculated as (Figure 1):

$$w(x) = w_{\max}\, e^{\left(-\frac{x^2}{2i_x^2}\right)} \tag{1}$$

$$V_S^* = \int w(x)\,dx = \sqrt{2\pi}\, i_x\, w_{\max} \Rightarrow w_{\max} = \frac{V_S^*}{i_x\sqrt{2\pi}} \tag{2}$$

where w_{max} is the maximum settlement in correspondence of the tunnel axis, i_x represents the half-width of the settlement trough, defined as the horizontal distance between the tunnel axis and the point of inflection of the settlement curve, and V^*_s is the total volume of the surface settlement trough (per unit length of tunnel), obtained by integrating Equation (1).

O'Reilly and New (1982), analysing field data from a series of tunnelling projects in relatively homogeneous soils, showed that i_x is proportional to the depth of the tunnel axis z_0:

$$i_x = K z_0 \tag{3}$$

The "width parameter" K depends essentially on the soil type: for coarse-grained soils varies from 0.25 to 0.45, with an average value $K = 0.35$ (Mair and Taylor, 1997).

O'Reilly and New (1982) also observed that the displacement vector is approximately directed toward the axis of the tunnel, or, in other words, that the horizontal displacement, u_h, may be calculated from the vertical settlement at the same location, w, by the following equation

$$u_h(x) = -\frac{x}{z_0} w(x) \tag{4}$$

A convenient reference parameter often adopted in design practice is the "ground volume loss" (V_S), which represents the volume of the surface settlement trough related to the nominal volume of the tunnel cross-section, while the "tunnel volume loss" (V_L), represents the closure of the excavation profile, normalised in the same way (D_f is the nominal diameter of the tunnel)

$$V_S = \frac{4\,V_S^*}{\pi D_f^2} \tag{5a}$$

$$V_L = \frac{4\,V_L^*}{\pi D_f^2} \tag{5b}$$

In perfectly undrained conditions (i.e., for an incompressible medium), the ground volume loss (V_S) is equal to the tunnel volume loss (V_L). For coarse-grained soils, however, the surface volume loss can be lower or higher than the tunnel volume loss if a dilative or contractive volumetric behaviour prevails, depending on the dilatancy angle (ψ) of the soil. Thus, the volume losses (V_S) is a function of the mechanical properties of the soil as well as of the construction method (i.e., the specific process of excavation and support installation).

Attewell & Woodman (1982) also inferred that the longitudinal settlement profile, along the tunnel axis, is well represented by the Gaussian cumulative probability distribution. Settlements evolve with the advancement of the excavation face and the steady-state condition is reached when the maximum settlement (w_{max}) is completely developed.

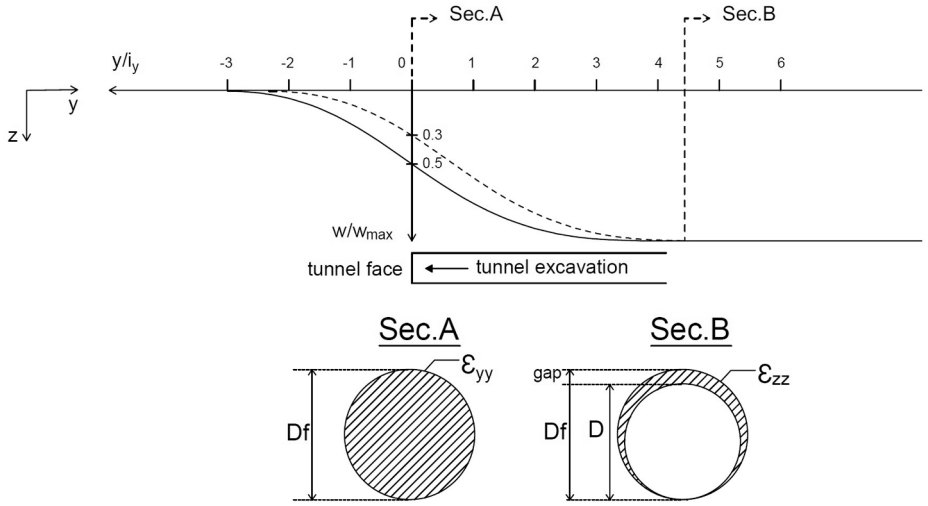

Fig. 3. Schematic of the two cross-sections considered for settlements prediction: Section A at the face, Section B at the steady-state.

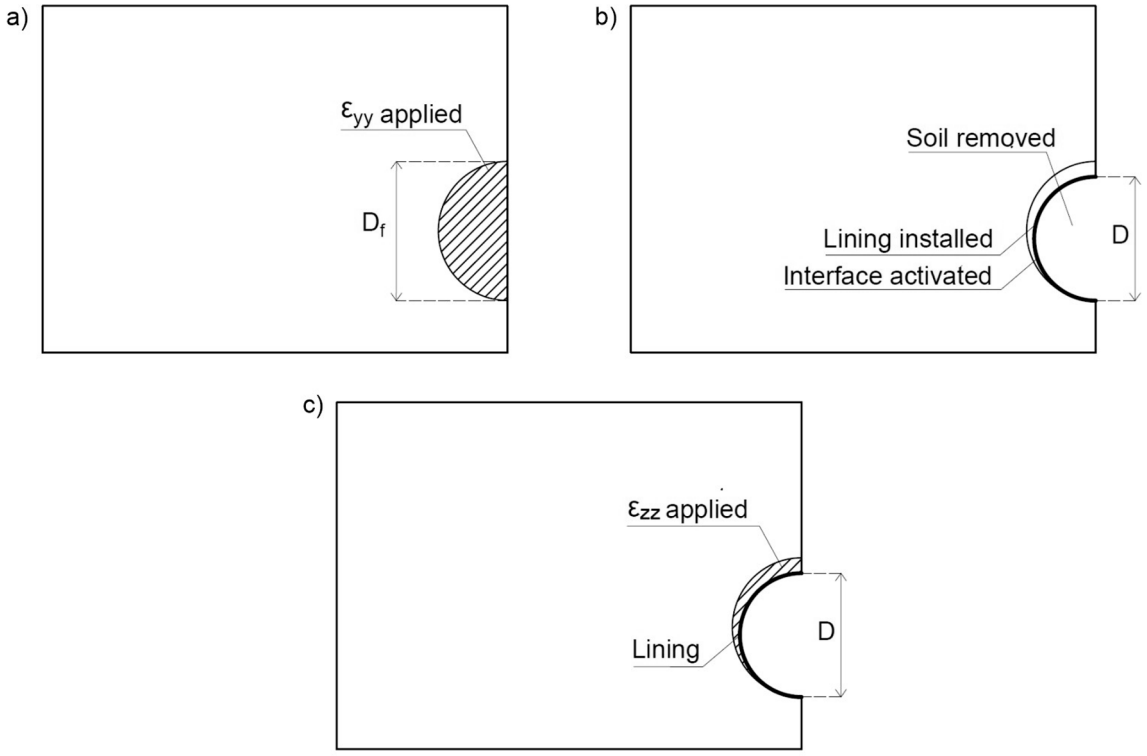

Fig. 4. Calculation stages: Phase 1, Section A (a), Phase 2 (b) and Phase 3, Section B (c).

Table 1
Summary of geometry data for the five case histories.

Tunnel	Country	z_0 [m]	D_f [m]	z_0/D_f [-]	z_w [m]	Main references
a. 2nd Heinenoord	NL	15.6	8.5	1.8	−1.5	(Möller and Vermeer, 2008)
b. Milan – M1 ext.	IT	11.5	6.54	1.8	−11.5	(Migliazza et al, 2009)
c. Cairo L2 – Lot.12	EGY	18.0	9.4	1.9	−3.0	(El-Nahhas and El-Mossallamy, 2009)
d. Cairo L2 – Lot.16	EGY	17.8	9.4	1.9	−1.9	(El-Nahhas et al., 2015)
e. Naples – L6	IT	17.3	8.15	2.1	−2.9	(Bilotta et al., 2017)

3. Finite element modelling

In the detailed design phase, the empirical approach is generally complemented by finite element numerical modelling, which is a very general and flexible approach, suited to model any soil mechanical behaviour, tunnel geometry and construction process.

This section focuses on FEM analysis of shield-driven tunnels in plane-strain conditions. All the analyses were performed by the software

Table 2
Summary of lining and shield data for the five case histories.

Tunnel	Method	s_r [m]	L_r [m]	Lining segments [Nr.]	D [m]	L_s [m]	gap [mm]
a. 2nd Heinenoord	Slurry	0.35	1.5	7	8.3	8.0	200
b. Milan – M1 ext.	EPB	0.30	1.4	n.a.	6.3	9.0	240
c. Cairo L2 – Lot.12	Slurry	0.40	1.5	7	9.15	9.0	250
d. Cairo L2 – Lot.16	Slurry	0.40	1.5	7	9.15	9.0	250
e. Naples – L6	EPB	0.30	1.7	9	7.85	n.a.	300

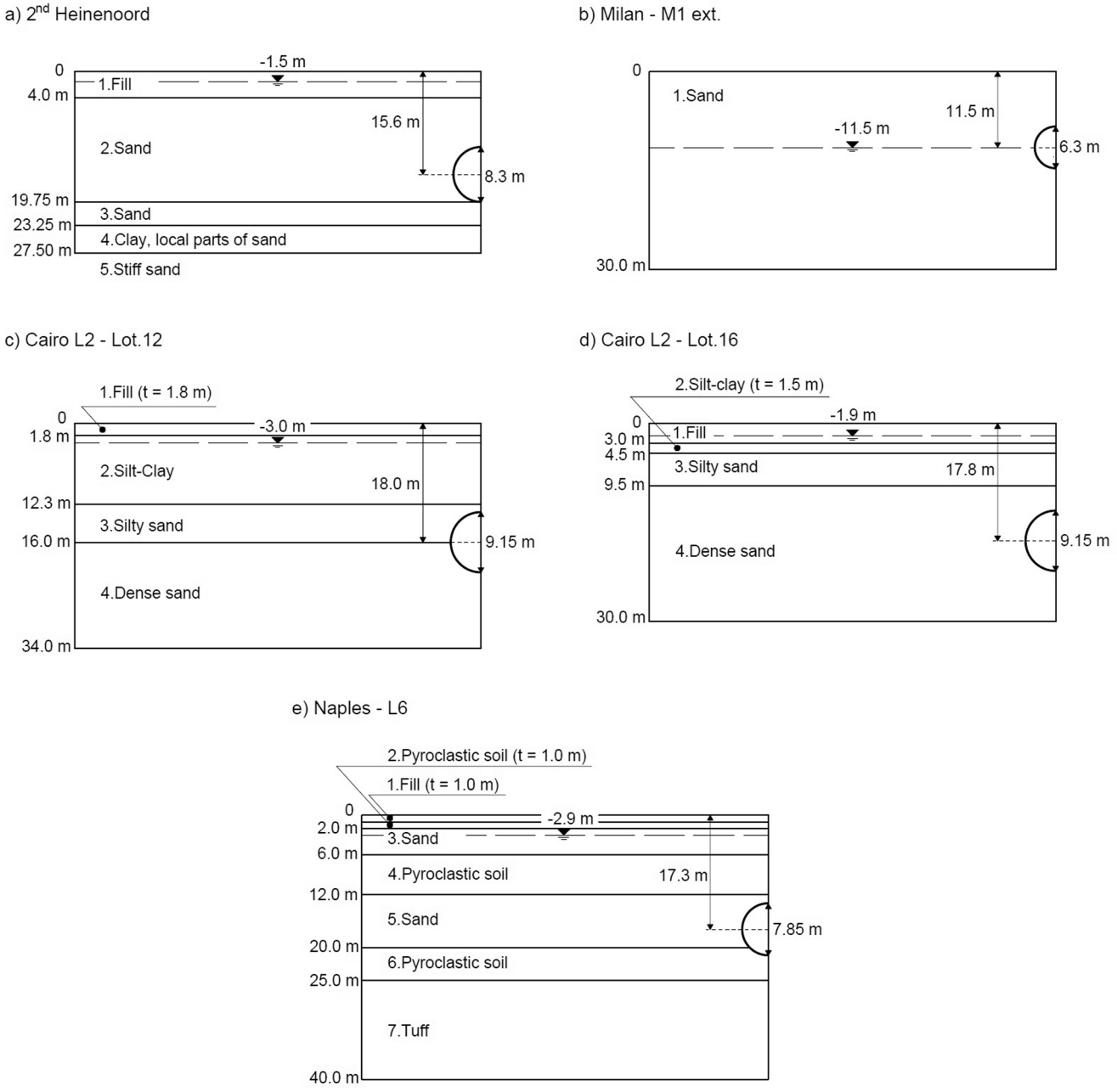

Fig. 5. Subsoil profiles and tunnel cross-sections: 2nd Heinenoord (a), Milan – M1 ext. (b), Cairo L2 – Lot.12 (c), Cairo L2 – Lot.16 (d) and Naples – L6 (e).

Plaxis 2D (Brinkgreve et al., 2017). A novel approach for 2D-modelling of tunnel excavation, called the "*Strain applied method*", has been developed, in which the three-dimensional effects induced by the actual boring process are simulated by applying specific strain distributions around the tunnel cross-section. The mechanical behaviour of the soil will be modelled by both a linear-elastic perfectly plastic model (*Mohr-Coulomb, MC*) and a more complex constitutive model with non-linear stiffness and isotropic hardening (*Hardening Soil* model with small strain stiffness*, HSs*); a more detailed description of this last model is given in the Appendix.

3.1. Mesh dimensions and boundary conditions

The typical situation to be modelled (Figure 2) is that of a single

Table 3
Soil parameters of the *MC* model for the five case histories.

Tunnel	Soil type	γ_{sat} [kN/m^3]	c' [kPa]	φ' [°]	ψ' [°]	υ' [-]	K_0 [-]
a. 2nd Heinenoord	Dense sand	20	0	35	0	0.3	0.47
b. Milan – M1 ext.	Sandy gravel	22	0	30	10	0.3	0.50
c. Cairo L2 – Lot.12	Silty sand/Dense sand	19/20	0	30/37	0	0.35/0.3	0.50/0.40
d. Cairo L2 – Lot.16	Silty sand/Dense sand	19/20	0	30/37	0	0.35/0.3	0.50/0.40
e. Naples – L6	Pyroclastic soil/Marine sand	16/18	0	37/37	0	0.2/0.2	0.40/0.40

Table 4
Soil parameters of the *HSs* model for the five case histories.

Tunnel	Soil type	G_0^{ref} [MPa]	E_{50}^{ref} [MPa]	$\gamma_{0.7}$ [-]	m [-]
a. 2nd Heinenoord	Dense sand	175	35	$5{\cdot}10^{-4}$	0.5
b. Milan – M1 ext.	Sandy gravel	250	48	$1{\cdot}10^{-4}$	0.4
c. Cairo L2 – Lot.12	Silty sand/Dense sand	116/170	20/35	$2.8{\cdot}10^{-4}$/$4.5{\cdot}10^{-4}$	0.5
d. Cairo L2 – Lot.16	Silty sand/Dense sand	116/170	20/35	$2.8{\cdot}10^{-4}$/$4.5{\cdot}10^{-4}$	0.5
e. Naples – L6	Pyroclastic soil/Marine sand	180/90	47/40	$1.9{\cdot}10^{-4}$/$1.3{\cdot}10^{-4}$	0.5

tunnel bored in a coarse-grained soil (depth of tunnel axis, z_0), with negligible disturbance of the initial pore pressure distribution (drained, hydrostatic conditions). Details on the specific case histories considered in this study are reported in the next Section 4.

The mesh dimensions (Figure 2a) are chosen in order that the artificial boundaries have negligible influence on the solution, particularly on extent and shape of the settlement trough. Tests with meshes of larger transversal size confirmed that the assumed width ($b/2 \approx 5D$) is satisfactory. The horizontal displacement along the vertical boundaries has been restrained, while the bottom boundary is completely restrained.

3.2. Tunneling simulation – The proposed "Strain applied method"

Plane strain methods currently utilized in engineering practice (i.e. *Convergence – Confinement method, Contraction method, Gap method, Grout Pressure,* etc.) can only predict the "final conditions" (or steady-state situation, away from the tunnel face) and typically require the calibration of a single parameter. Instead, in the *Strain applied method* herein introduced two different cross-sections, or excavation phases, can be represented: the stress and strain conditions at the excavation face (Section A) and at the steady-state conditions (Section B).

The schematic of the two modelling phases, corresponding to two different "control sections" along the longitudinal profile of the surface settlement, is shown in Figure 3. Attewell et al. (1986) suggested that, for open-face tunnelling, the settlement directly above the tunnel face (Section A) is almost equal to half the maximum final settlement, 0.5 w_{max} (Figure 3, solid line). However, surface settlements in Section A can be significantly lower for closed-face shield, provided that the face pressure is regularly maintained (Figure 3, dashed line). Based on monitoring data, Mair and Taylor (1997) found that settlements as low as 0.25–0.3 w_{max} are typical for closed-face tunnelling in coarse-grained soil.

The 3D effects of excavation face advance can be accounted for by properly calibrating the tunnel volume losses, obtained by imposing suitable strains to a group of soil elements. The magnitude of these strains is treated as a "calibration parameter" of the procedure, to be back calculated in order to fit the measured settlements or to impose the expected ground volume loss V_S.

The main stages of the proposed calculation method are summarised in Figure 4. The final effect of the whole excavation process is the result of the volume losses imposed at the two control sections.

In order to simulate the stress release at the tunnel face, Sec. A (Figure 4a), it is possible to apply an in-plane isotropic deformation $\varepsilon_{xx} = \varepsilon_{zz}$ to the soil volume to be excavated ($\pi D_f^2/4$): a volume reduction must be produced; therefore, the imposed strains are negative. A similar effect can be obtained, by applying a negative strain in the out-of-plane direction, ε_{yy}, as generally done in the following analyses. In the last case, the plane strain model prevents any out-of-plane deformation and, therefore, the effect is to generate a positive (tensile) stress, σ_{yy}, which in turn induces a uniform negative in-plane deformation (shrinking) $\varepsilon_{xx} = \varepsilon_{zz}$.

Note that for a linear elastic model the in-plane strains are simply proportional, by the Poisson coefficient ν, to the imposed longitudinal strain ε_{yy} (i.e., $\varepsilon_{xx} = \varepsilon_{zz} = \varepsilon_{yy}/\nu$). When the non-linear *HSs* model is used for the soil core to be excavated, a further effect must be considered. In fact, the unloading produced by the imposed ε_{yy} is accompanied by a reduction in stiffness of the soil core, proportional to the minimum principal stress $\sigma'_3 \approx \sigma'_{yy}$. This effect can be accepted in that it can represent the likely consequence of the remoulding of the soil around the excavation head.

After the removal of the soil elements inside the tunnel section and the activation of the lining shell (Figure 4b), the soil-lining gap tends to close and the steady-state conditions are reached. This further volume loss is simulated by applying a ε_{zz} strain to a moon-shaped annulus of "disturbed soil" (Figure 4c). This annulus is of variable thickness, in fact, it represents the real "ground-lining gap" (distance between the extrados of the lining and the excavation profile) with maximum value at the crown and minimum (zero) at the invert. It is instrumental to model the tail void, the effect of the conical shield and of the possible overcutting, that is to say the main sources of tunnel volume loss, V_L. A confirmation for the particular shape assumed for the gap can be found in Franza et al. (2019), where a distinction is made between the deformation pattern around the tunnel depending on the soil type: in coarse-grained soil the ground loss appears particularly localized at the tunnel crown, therefore producing mainly vertical deformations.

The lining is represented by a ring of beam elements, having the equivalent-stiffness of the precast segmental lining, connected to the soil

Table 5
Parameters for the empirical approach (Gaussian curves).

Tunnel	$w_{Sec.A}$ [mm]	$w_{Sec.B}$ [mm]	i_x [m]	$K = i_x/z_0$ [-]	$V_{S\ Sec.A}$ [%]	$\Delta V_{S\ Sec.B}$ [%]	$V_{S\ tot}$ [%]	$V_{S\ Sec.A}/V_{S\ tot}$ [%]
a. 2nd Heinenoord	4	26	6.2	0.40	0.11	0.61	0.72	17.5
b. Milan – M1 ext.	7.5	13.6	5.2	0.45	0.29	0.24	0.53	61.5
c. Cairo L2 – Lot.12	2	11	7.2	0.40	0.05	0.23	0.29	21.3
d. Cairo L2 – Lot.16	6	18	7.7	0.40	0.17	0.33	0.50	36.0
e. Naples – L6	1.8*	6	7.8	0.45	0.07	0.16	0.23	32.0

* Estimated as 0.3 $w_{Sec.B}$.

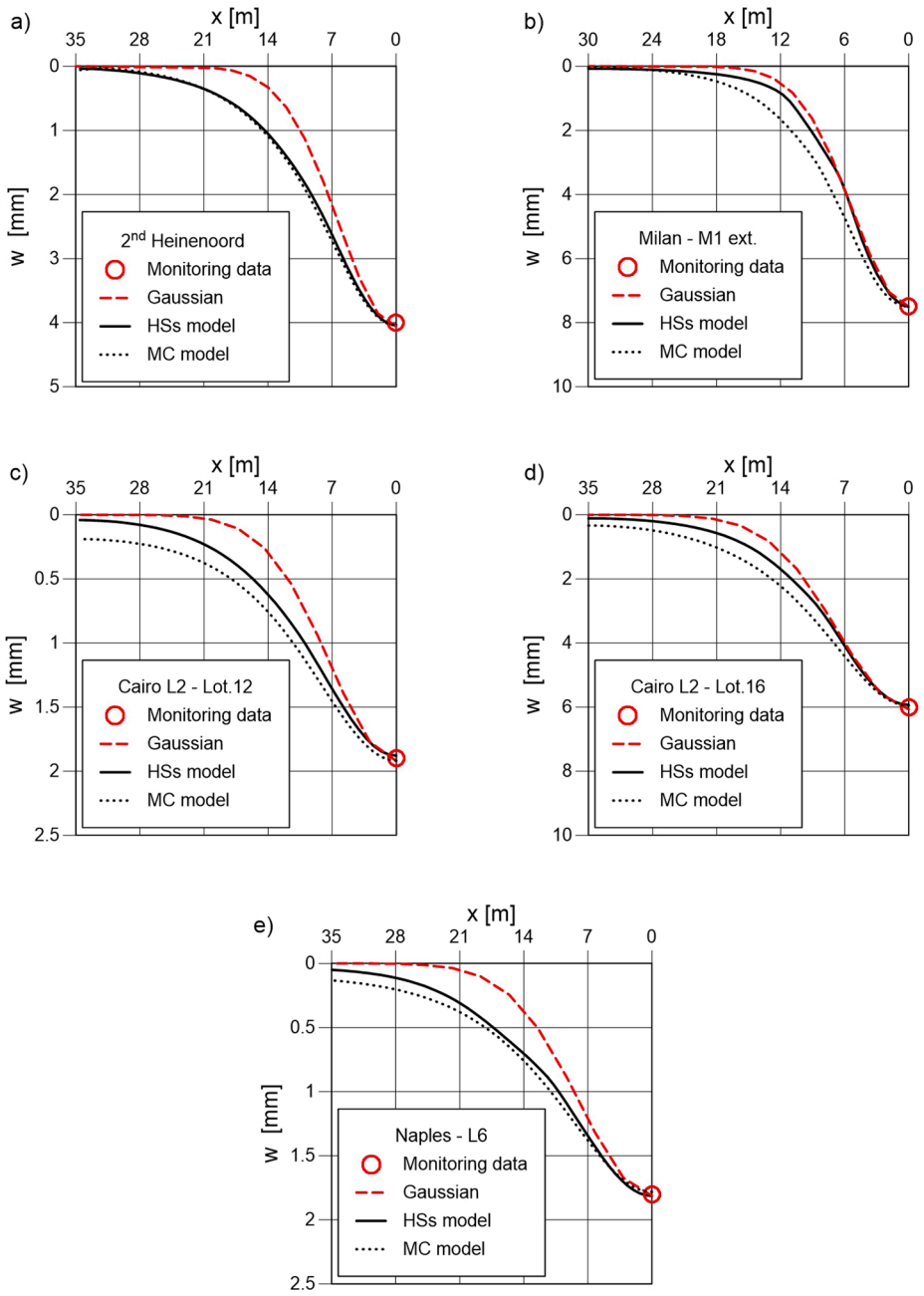

Fig. 6. Comparison of measured and computed (*MC* and *HSs* model) surface settlement troughs at the tunnel face: 2nd Heinenoord (a), Milan – M1 ext. (b), Cairo L2 – Lot.12 (c), Cairo L2 – Lot.16 (d) and Naples – L6 (e).

clusters by interface elements (same elasto-plastic parameters of the soil clusters).

The modelling procedure can be summarized in the following phases:

Phase 0 – Geostatic load: initial equilibrium conditions, characterized by given K_0 stress ratio and water table elevation.
Phase 1 – Section A: an out-of-plane strain ε_{yy} (Figure 4a) is applied to the excavation section (diameter, D_f) simulating the effects of the tunnel volume loss (stress release) at face ($V_{L,Sec.A}$) and the remoulding of the soil. At the end of this calculation step, the corresponding surface maximum settlement and surface volume loss are obtained (w_{SecA}, $V_{S,Sec.A}$).
Phase 2 – Lining installation: within the extrados of the lining (diameter, D), the soil is excavated, the pore pressure is removed and the lining ring is installed (Figure 4b).
Phase 3 – Section B: a vertical strain ε_{zz} (Figure 4c) is applied to the ground-lining gap simulating the additional volume loss due to the gap closure ($\Delta V_{L,Sec.B}$). The final increment in settlement and surface volume loss, far from the excavation face (steady-state conditions), are obtained (w_{SecB}, $\Delta V_{S,Sec.B}$).

In terms of computational steps, it has been found convenient to separate Phase 2 and Phase 3, although in the effective construction process, they can be considered as a single phase.

In the following, the two strain parameters (ε_{yy}, ε_{zz}) will be back-calculated ("calibrated") in order to fit the monitoring data of five well-documented case histories in greenfield condition (see Section 4).

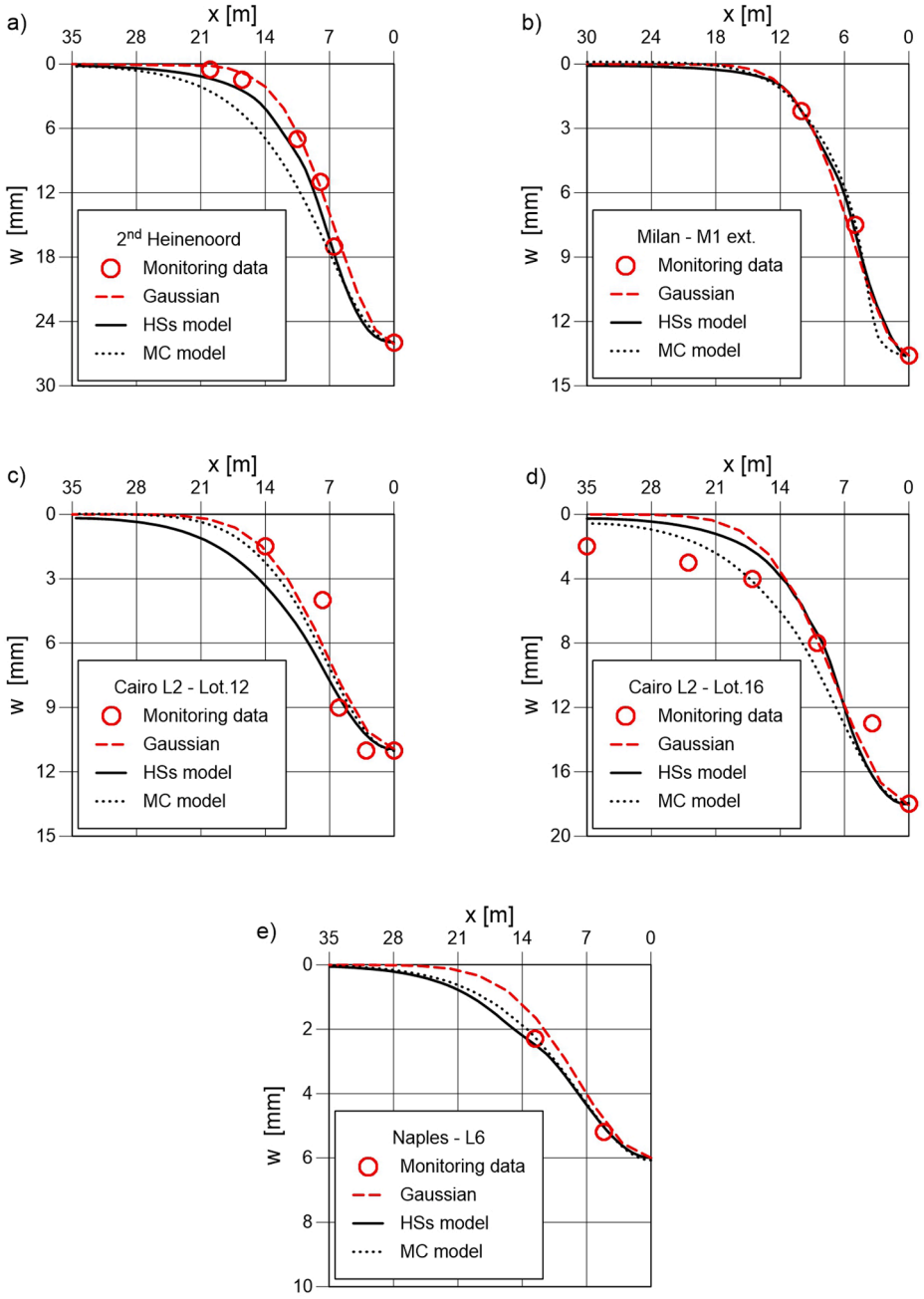

Fig. 7. Comparison of measured and computed (*MC* and *HSs* models) surface settlement troughs at the steady-state: 2nd Heinenoord (a), Milan – M1 ext. (b), Cairo L2 – Lot.12 (c), Cairo L2 – Lot.16 (d) and Naples – L6 (e).

The overall results of the numerical modelling can summarized by the following output parameters: the surface volume loss at the face, $V_{S,Sec.A}$, and the increment of the surface volume loss at the steady-state condition, $\Delta V_{S.Sec.B}$. The total volume loss at ground surface, at the end of the boring process, is given by $V_{S.Tot.} = V_{S,Sec.A}+\Delta V_{S.Sec.B}$.

4. Case histories considered in this study

Five case histories were selected to test the performance of the aforementioned modelling approach by comparison of computed results with field measurements. All the case studies refer to shallow tunnels (depth of tunnel axis, z_0, in the range 11.5–18.0 m, diameter, D, in the range 6.3–9.15 m, with a z_0/D ratio of 1.8–2.2) bored with EPB or Slurry-shield machines in greenfield condition. All tunnels were excavated in coarse-grained soils, although in some cases also different soil types were present below or above the tunnel depth. For all the cases a well detailed description was found in the literature, both for the geotechnical parameters as well as for the settlements data. A brief description of each case study follows.

The Second Heinenoord Tunnel (2nd Heinenoord), case (a), was bored by means of a Slurry-Shield TBM in a layered sand deposit overlaying a sandy-clay layer few meters below the tunnel invert (Bakker et al., 1999; van Jaarsveld et al., 1999; Möller and Vermeer, 2008). The Milan M1 extension (Milan – M1 ext.), case (b), was bored by an EPB-shield machine in a homogeneous deposit of sandy-gravels (Migliazza et al, 2009). Two instrumented sections (Lot.12 and Lot.16) of the Cairo L2 tunnel represent, respectively, the cases (c) and (d); they were excavated by a Slurry-Shield. The Cairo L2 line passes through medium dense to very dense sands overlaid by a finer cohesive transition layer (El-Nahhas and El-Mossallamy, 2009; El-Nahhas et al., 2015). The last

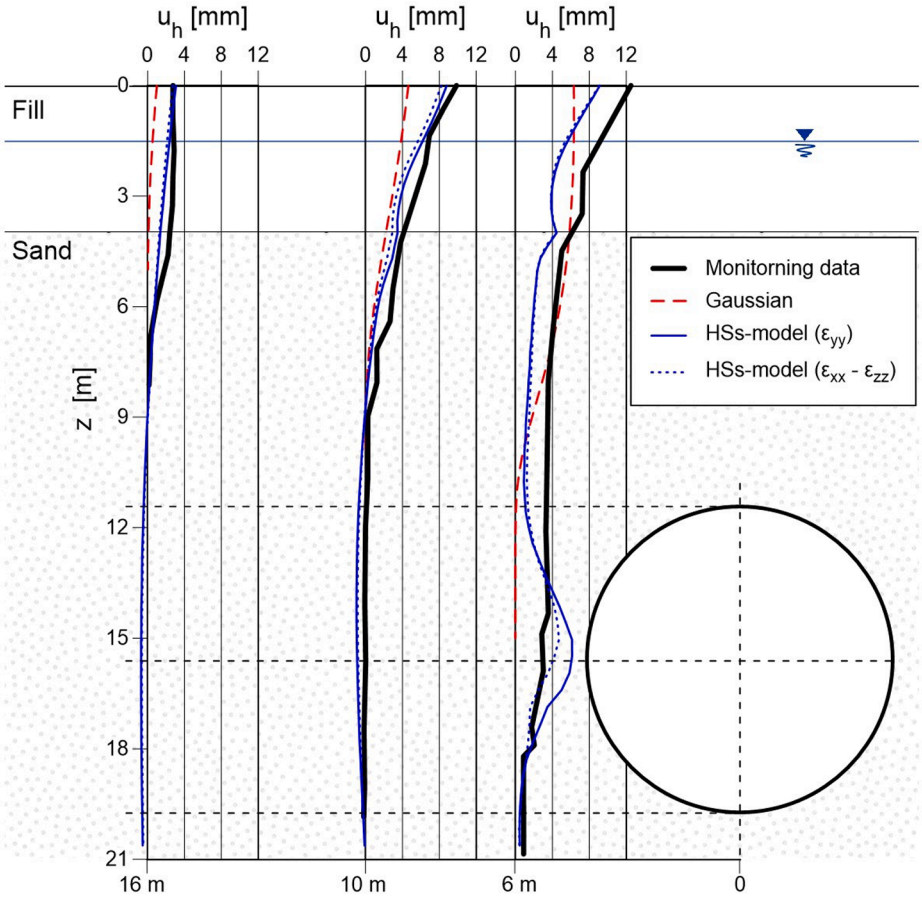

Fig. 8. Comparison of measured and computed (*HSs* ε_{xx}-ε_{zz} and *HSs* ε_{yy} model) horizontal displacements with depth at the steady-state at a distance of 6, 10 and 16 m from the axis of 2nd Heinenoord tunnel.

case (e) is the Naples L6 tunnel, bored by an EPB-shield TBM in alternated pyroclastic soils and marine sands (Bilotta and Russo, 2012; Bilotta et al., 2017; Celentano et al., 2017).

In all cases, the water table is close to the ground surface, only for Milan – M1 ext. the water table is at the same elevation of the tunnel axis. Moreover, the installed segmental linings are endowed with watertight joints and can be considered as an impervious boundary.

Table 1 lists the main geometry data for the five case histories: z_0 is the depth of the tunnel axis, D_f the excavation diameter and z_w the depth from ground surface of the piezometric surface.

Table 2 summarizes the parameters of the lining and the shield characteristics: s_r is the lining thickness, L_r the lining ring length, D the extrados diameter of the lining, L_s the shield length; the "gap" parameter represents the difference between the nominal diameter of excavation and the external diameter of the lining.

Figure 5 shows the typical subsoil profile and the tunnel geometry of the five case studies.

For each case, it is possible to represent the soil behaviour both by an elasto-plastic model (*Mohr-Coulomb*, *MC*) and by the *Hardening Soil* model with small strain stiffness (*HSs*), first described in Benz (2007). The mechanical parameters utilized for the main sandy layers of each case study are briefly summarized in the following. The reader should refer to the mentioned literature for further details and insight into the case studies. Table 3 lists the soil parameters of the *MC* model inferred from geotechnical investigations: γ_{sat} total unit weight, c' cohesion, φ' friction angle, ψ' dilatancy angle, υ' Poisson's ratio and K_0 coefficient of earth pressure at rest. The additional geotechnical parameters for the *HSs* model are reported in Table 4: small-strain shear modulus (G_0^{ref}) at the reference confining pressure (p^{ref} = 100 kPa), reference secant stiffness modulus (E_{50}^{ref}), shear strain ($\gamma_{0.7}$) at which secant shear modulus $G_s = 0.7G_0$, parameter for stress-stiffness law (m).

5. Comparison of settlement results

The reliability of the proposed FEM modelling approach for the prediction of settlements was assessed, essentially, by comparing the computed settlement troughs with the empirical predictions (Gaussian curve, see Equation (1)). The Gaussian curve was not used for settlement prediction but simply for fitting the monitoring data, imposing that the curve passes through the point of maximum settlement measured above the tunnel axis ($w_{Sec.B}$). However, due to the limited data available in the cross-section of the tunnel face (Section A), the shape of the settlement trough in the transversal direction was assumed fixed, i.e., considering also for the tunnel face the same width parameter (K) calibrated for the steady-state condition (Section B).

Table 5 reports the parameters of the Gaussian curves obtained by field data fitting; $w_{Sec.A}$ is the surface settlement measured above the tunnel face, $w_{Sec.B}$ is the maximum final settlement measured in steady-state condition.

In the following subsections, the effects of the specific soil constitutive model on the induced settlements are discussed; the results are presented for both the face (Subsection 5.1) and the steady-state conditions (Subsection 5.2).

5.1. Face conditions (Section A)

Figure 6 plots the results at the tunnel face. The settlement troughs estimated by the FEM modelling are not always in agreement with the empirical profile. In particular, the calculated profiles (*MC* and *HSs* model) for cases 6a, 6c and 6e tend to overestimate the width of the

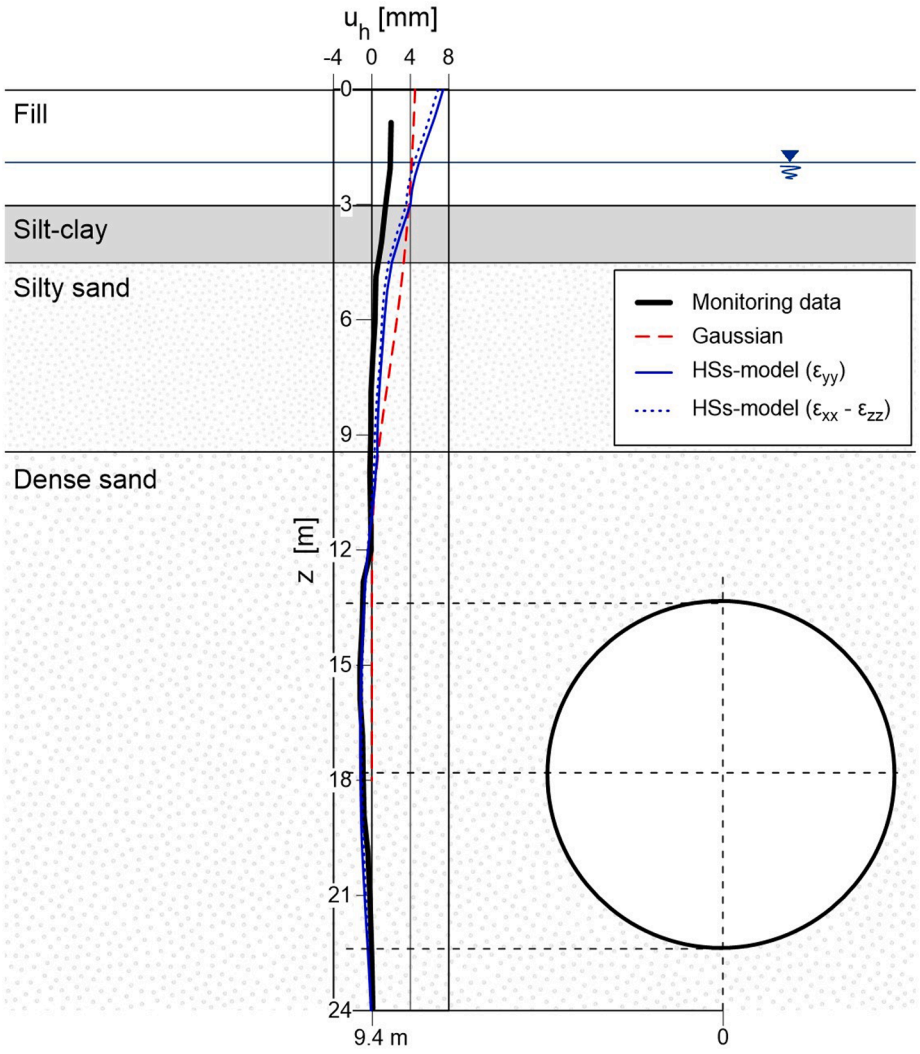

Fig. 9. Comparison of measured and computed (*HSs* ε_{yy} and *HSs* $\varepsilon_{xx} - \varepsilon_{zz}$) horizontal displacements with depth at the steady-state at 6, 10 and 16 m from the axis of Cairo L2 – Lot.16 tunnel.

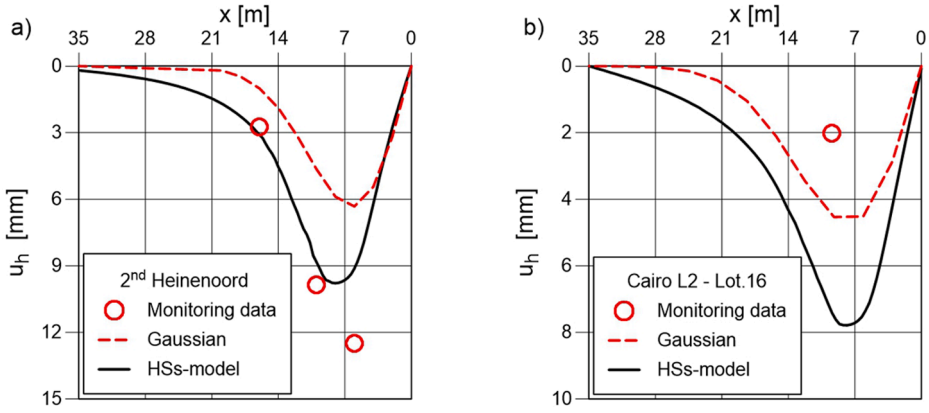

Fig. 10. Comparison of measured and computed (*HSs* model) surface horizontal displacements at the steady-state: 2nd Heinenoord (a) and Cairo L2 – Lot.16 (b).

empirical trough, a good agreement is found only for cases 6b and 6d, particularly if the non-linear *HSs* model is utilized. However, as already remarked, the Gaussian curve does not represent an interpolation of measured settlements at different distance from the tunnel axis but is only anchored to a single point: the maximum settlement $w_{Sec.A}$, above the tunnel axis.

5.2. Steady-state conditions (Section B)

Figure 7 shows the settlement profiles obtained by the empirical (Gaussian) and numerical (FEM) approaches for the steady-state conditions, when the maximum final settlement is completely developed. The numerical results for both the constitutive models are compared

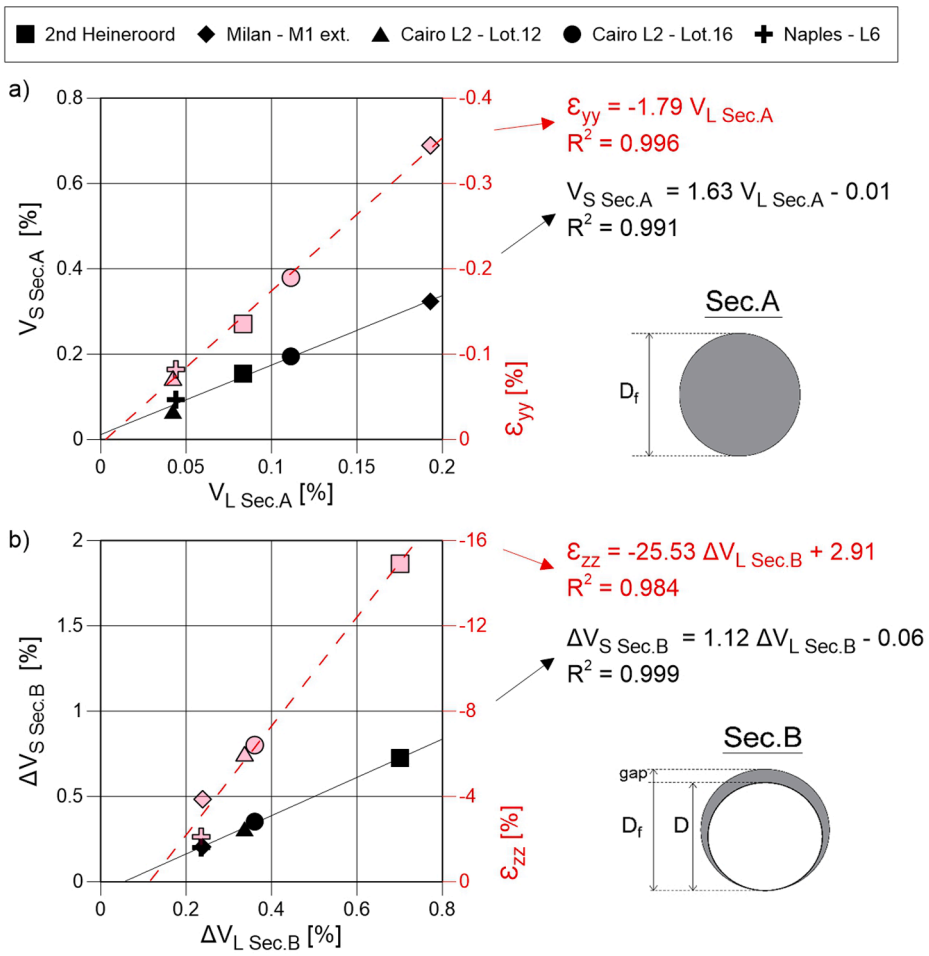

Fig. 11. Computed ground volume loss at the surface against tunnel volume loss for each case history: Section A (a) and Section B (b). The equations of linear regression are given in the $V_{L\ Sec.A}$-$V_{S\ Sec.B}$, $\Delta V_{L\ Sec.A}$-ε_{yy}, $\Delta V_{L\ Sec.A}$-$\Delta V_{S\ Sec.B}$ and $\Delta V_{L\ Sec.A}$-ε_{zz} planes.

Table 6
Computed volume losses at the surface and at the tunnel axis for the five case histories.

	$V_{S\ Sec.A}$ [%]	$V_{L\ Sec.A}$ [%]	$\Delta V_{S\ Sec.B}$ [%]	$\Delta V_{L\ Sec.B}$ [%]	$V_{S\ tot}$ [%]	$V_{L\ tot}$ [%]	$V_{S\ Sec.A}/V_{S\ tot}$ [-]	$V_{S\ tot}/V_{L\ tot}$ [-]
a. 2nd Heinenoord	0.15	0.08	0.72	0.70	0.88	0.78	0.17	1.13
b. Milan – M1 ext.	0.32	0.19	0.21	0.24	0.53	0.43	0.60	1.23
c. Cairo L2 – Lot.12	0.07	0.04	0.31	0.34	0.38	0.38	0.18	1.00
d. Cairo L2 – Lot.16	0.20	0.11	0.35	0.36	0.55	0.47	0.36	1.17
e. Naples – L6	0.09	0.04	0.20	0.23	0.29	0.28	0.31	1.04

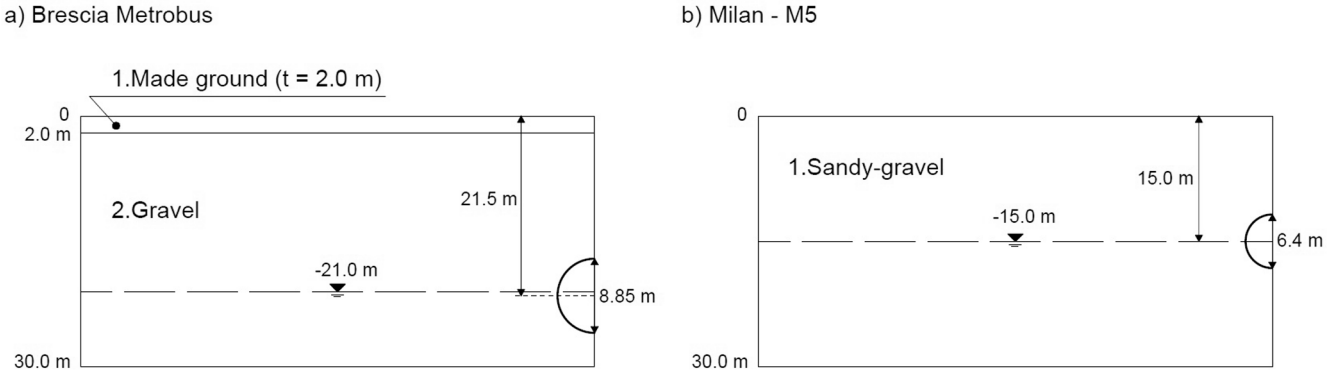

Fig. 12. Subsoil profile and tunnel cross-section: Brescia Metrobus (a) and Milan – M5 (b).

Table 7
Summary of geometry data for Brescia Metrobus and Milan – M5.

Tunnel	z_0 [m]	D_f [m]	z_0/D_f [-]	z_w [m]	Main reference
a. Brescia Metrobus	21.5	9.15	2.3	−21.0	(Sanzeni et al., 2017)
b. Milan – M5	15.0	6.70	2.2	−15.0	(Fargnoli et al., 2015)

Table 8
Summary of lining and shield data for Brescia Metrobus and Milan – M5.

Tunnel	Method	s_r [m]	L_r [m]	Lining segments [Nr.]	D [m]	L_s [-]	Gap [mm]
a. Brescia Metrobus	EPB	0.35	n.a.	7	8.85	n.a.	300
b. Milan – M5	EPB	0.30	1.4	6	6.40	10	300

with field data.

The first observation concerns the results obtained by the *HSs* model, that are in better agreement with both the measurement points and the empirical curve, with respect to the results for Section A. Instead, the settlement profiles obtained by the *MC* model (in particular, for cases 7a and 7d) tend to slightly overestimate the width of the settlement trough, and consequently also the volume loss, as already noticed by Addenbrooke et al. (1997) and Hejazi et al. (2008).

Therefore, it seems quite affordable, based on available data, to get a good prediction of the final settlement trough while the intermediate stages present greater challenges. An imposed strain method based on a single calibration parameter (e.g., the application of ε_{yy} strain, as in the previous calculation Phase 1) could be considered as a convenient alternative to the proposed method. However, it was found that the two-parameters modelling approach, besides representing the actual deformation mechanism better, gives more satisfactory results (Schiena, 2020).

Table 9
Soil parameters of the *HSs* model for Brescia Metrobus and Milan – M5.

Tunnel	Soil type	γ_{sat} [kN/m^3]	c' [kPa]	φ' [°]	ψ' [°]	υ' [-]	K_0 [-]	G_0^{ref} [MPa]	E_{50}^{ref} [MPa]	$\gamma_{0.7}$ [-]	M [-]
a. Brescia Metrobus	Gravel	20	0	36	0	0.3	0.41	210	65	$1{\cdot}10^{-4}$	0.4
b. Milan – M5	Sandy gravel	20	0	33	0	0.3	0.45	250	48	$1{\cdot}10^{-4}$	0.4

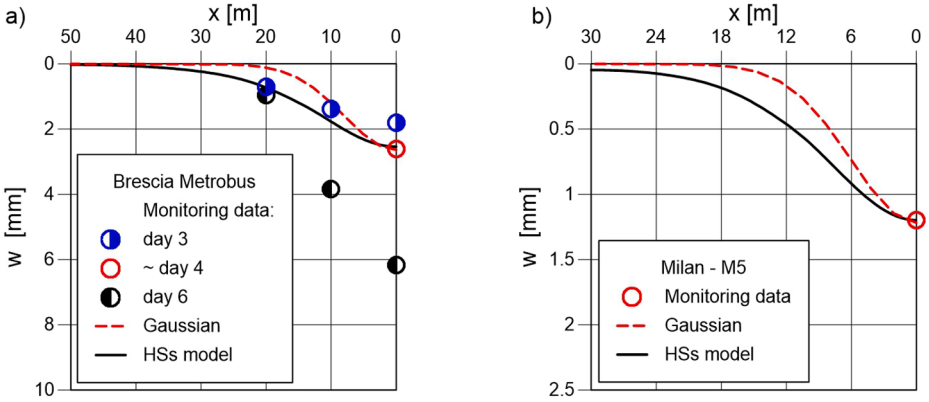

Fig. 13. Comparison of measured and computed (*HSs* model) surface settlement troughs at the face cross-section (Section A): Brescia Metrobus (a) and Milan M5 (b).

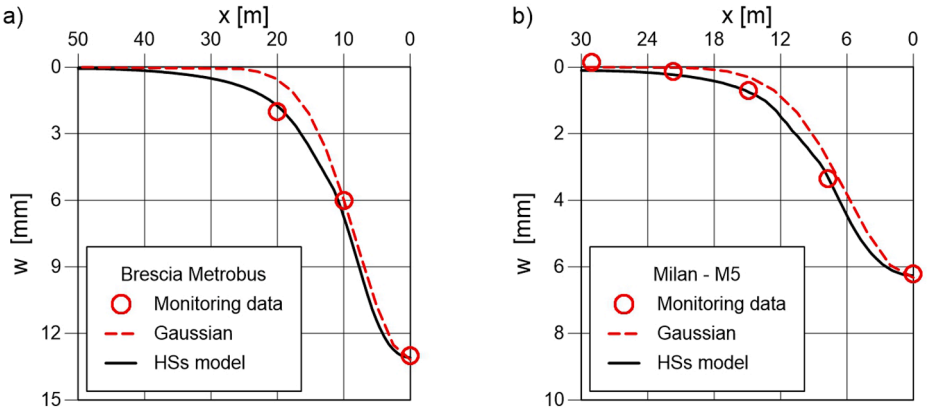

Fig. 14. Comparison of measured and computed (*HSs* model) surface settlement troughs at steady-state (Section B): Brescia Metrobus (a) and Milan – M5 (b).

Table 10
Parameters for the empirical approach (Gaussian curve): Brescia Metrobus and Milan – M5 tunnels.

Tunnel	$w_{Sec.A}$ [mm]	$w_{Sec.B}$ [mm]	i_x [m]	$K = i_x/z_0$ [-]	$V_{S\ Sec.A}$ [%]	$\Delta V_{S\ Sec.B}$ [%]	$V_{S\ tot}$ [%]	$V_{S\ Sec.A}/V_{S\ tot}$ [%]
a. Brescia Metrobus	2.6	13	8.0	0.37	0.08	0.32	0.40	26.5
b. Milan M5	1.2	6.2	6.0	0.4	0.05	0.22	0.27	25.0

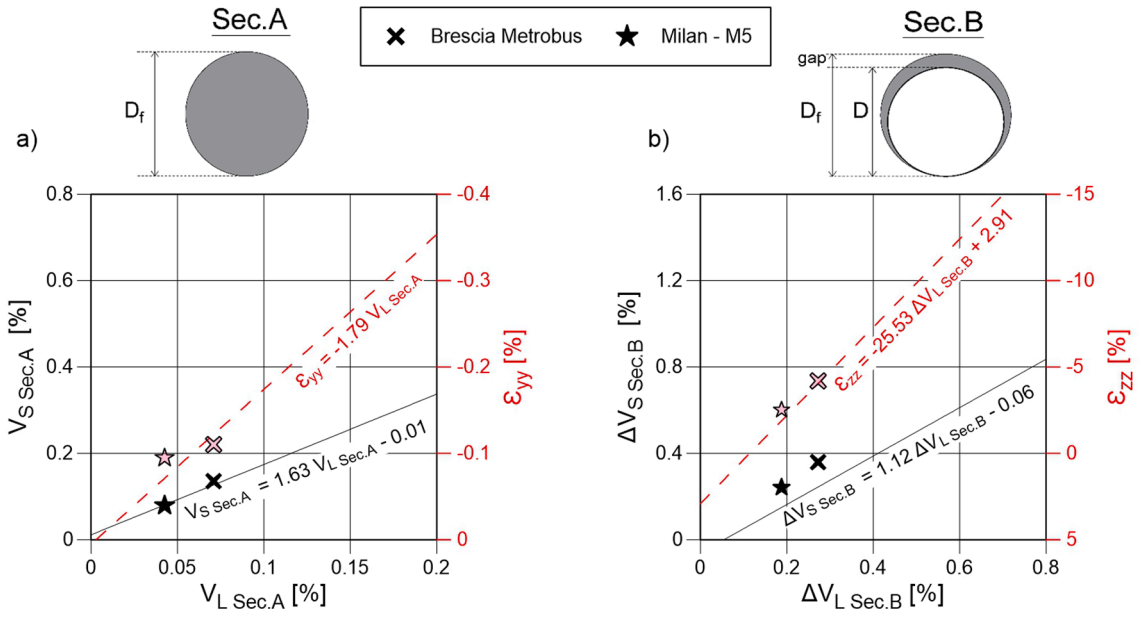

Fig. 15. Computed volume loss at the surface against tunnel volume loss for Brescia Metrobus and Milan – M5, compared to the average trend of the previous cases: Section A (a) and Section B (b).

6. Comparison of horizontal displacements

Vertical profiles of horizontal displacements were available only for two of the analysed case studies (i.e., 2nd Heinenoord and Cairo L2 – Lot. 16). Since the calibration of the ε-method was performed with respect to the maximum settlement at ground surface, an inspection of the horizontal displacements within the soil can be considered as a further validation of the method.

For the 2nd Heinenoord case, three monitoring sections were implemented: located 6, 10 and 16 m apart from the tunnel axis. Figure 8 shows that FEM-simulated and measured displacements are in very good agreement, at least for the two furthest verticals, while for the vertical at 6 m distance, a good agreement is found only below the invert. The influence of two possible methods for applying the volumetric strains in Phase 1 (i.e., the basic ε_{yy} and the alternative ε_{xx}-ε_{zz} method, as defined in Section 3) were also investigated. At the tunnel level, the displacement profiles calculated by both the methods exhibit a bulging towards the excavation, with a maximum at the sidewalls elevation, which is nearly absent in the real displacement profile. In the portion between sidewalls and crown elevations the curves of the simulated settlements show an inversion in gradient. Finally, above the crown elevation, the calculated displacements are less than the recorded ones, but the trend is however consistent. In other words, the horizontal displacements appear more localized around the cavity in the FEM model, while they are more uniformly distributed in the real case.

A significant difference between the two possible methods for applying isotropic volumetric strains can be observed in the magnitude of bulging, with ε_{yy} producing the largest displacements owing to the stiffness reduction induced by the out-of-plane prescribed strains. With this respect, the ε_{xx}-ε_{zz} method seems in better agreement with real data. A comparison with the calculated profiles in Möller and Vermeer (2008) shows that the herein proposed ε-method (either applying ε_{yy} or ε_{xx}-ε_{zz}) induces a displacement distribution in the soil similar to the *Contraction* and the *Stress Reduction* methods and different from the *Grout Pressure* method.

For the second case (i.e., Cairo L2 – Lot.16), horizontal displacement data are available only for a single vertical located at 9.4 m from the tunnel axis (Figure 9). The vertical profile from FEM analysis closely resembles the middle profile of the 2nd Heinenoord case, which is located at a similar distance (10 m) from the tunnel axis, but in this case the agreement with monitoring data seems less accurate: while the simulated and measured curves are in very good agreement below 10 m depth (i.e., 7.8 m above the tunnel axis), they substantially diverge at shallow depth. However, for the Cairo L2 case, a mismatch with monitoring data was observed also in the settlement trough (Figure 7d).

A possible explanation to these findings can rely on a not-optimal estimation of the *HSs* model parameters or more likely, on the influence of the consolidation process that could have taken place in the silt–clay layer, close to the surface, also considering that the water table is just 1.9 m below the ground surface. In fact, the non-zero settlements observed at a considerable distance from the tunnel axis are consistent with the superimposed effect of uniformly distributed consolidation settlement of the silt–clay layer In El-Nahhas et al. (2015), the horizontal displacement profile predicted by the Contraction method and the *HSs* model, is compared with the actual displacements. The two curves are generally in good agreement for what concerns the displacements at ground surface. On the contrary, the FEM-3D model by El-Nahhas et al. (2015) fails to capture the displacement distribution at the tunnel depth, well predicted by the 2D model in this paper.

A comparison between calculated and measured horizontal displacements at ground surface is shown in Figure 10. The Gaussian curve was calculated from settlement data after Equation (4) in Section 2. For the 2nd Heinenoord case, the FEM model offers a better estimation than the empirical Gaussian approach, but underestimates the horizontal

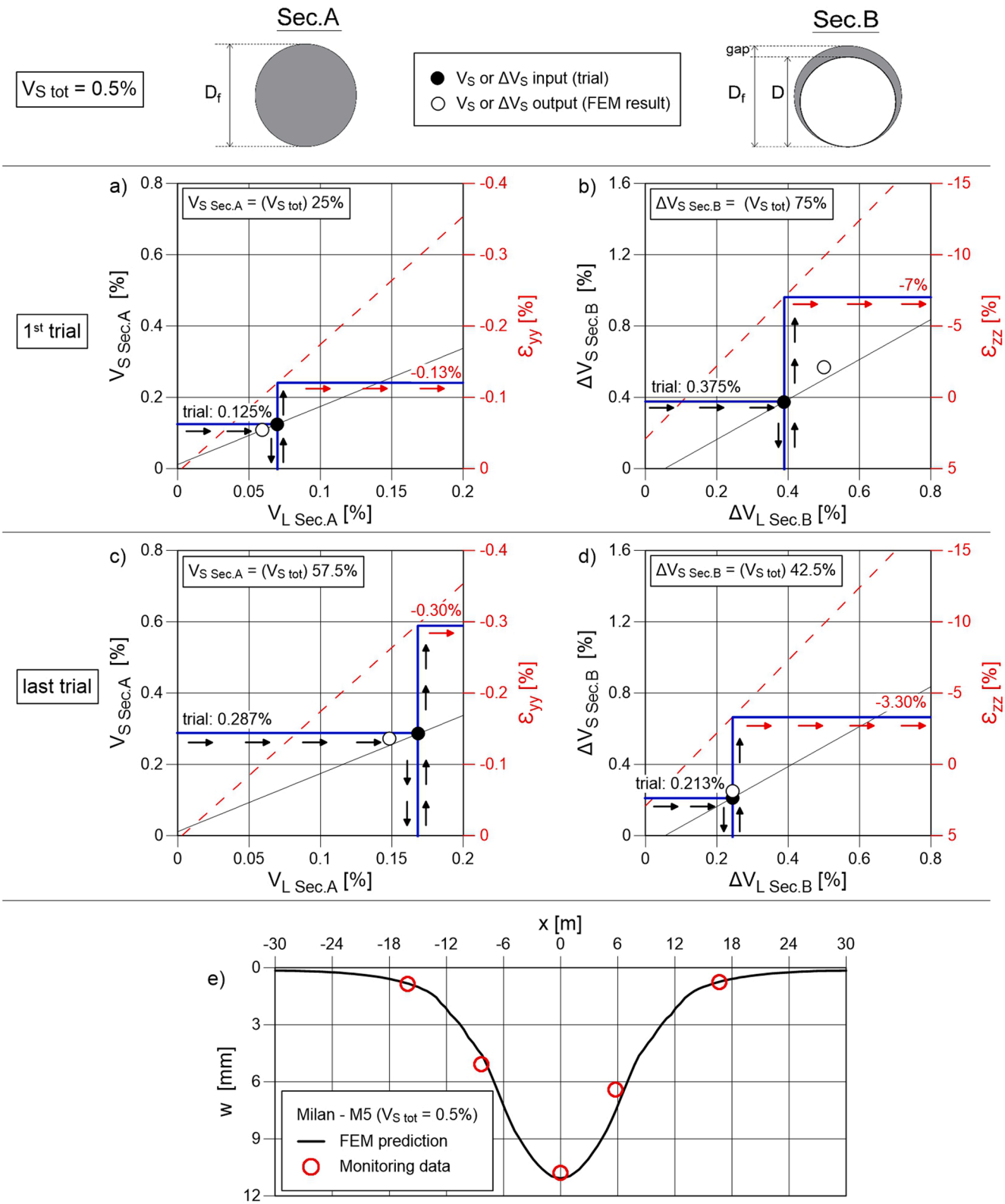

Fig. 16. Application of the "Predictive lines" of Equations (6-9) for obtaining the imposed strain to feed the FEM model after a trial-and-error iterative procedure (a, b, c, d); verification of the FEM prediction against the monitoring data (Milan – M5 monitoring section S897.3, Fargnoli et al., 2013).

displacements near the tunnel. For the Cairo L2 – Lot.16 case, both the FEM model and the Gaussian approach are less satisfactory. It seems that the Gaussian curve would fit better the monitoring data if a lower i_x value were adopted and the contribution of consolidation settlement excluded.

7. Comparative analysis of the volume losses

This section provides a comparative analysis of the different case histories in terms of computed volume losses. Figure 11 plots the ground volume loss at the surface (V_S) against the volume loss at the tunnel axis

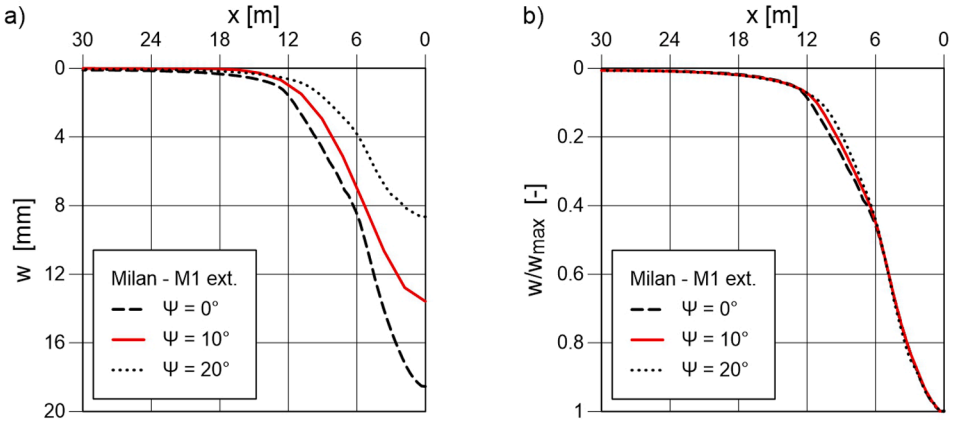

Fig. 17. Surface settlement troughs (a) and normalized surface settlement troughs (b) for different values of dilatancy angle ($\psi = 0°$, $\psi = 10°$, $\psi = 20°$).

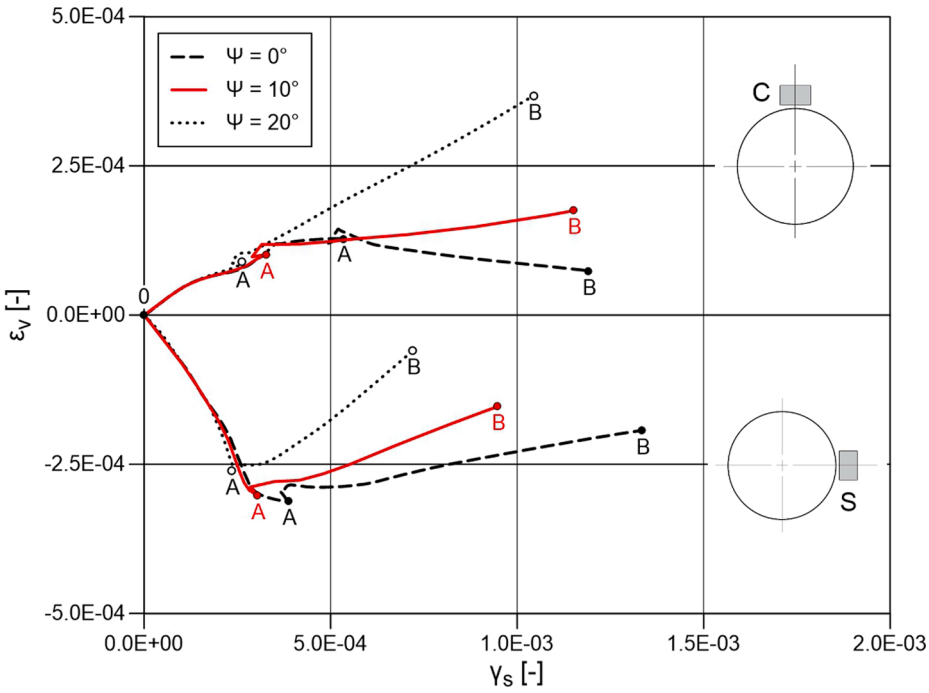

Fig. 18. Volumetric strain ε_v related to deviatoric strain γ_s at the crown and at the sidewall for different values of dilatancy angle ($\psi = 0°$, $\psi = 10°$, $\psi = 20°$).

(V_L) after the imposition of prescribed strains.

Figure 11a (face condition, Section A) shows the amount of surface volume loss $V_{S\ Sec,A}$ as a function of tunnel volume loss $V_{L\ Sec.A}$, given by the imposed ε_{yy}. The corresponding parameters for the steady-state condition (Section B) are represented in Figure 11b. The excavation of the soil inside the tunnel diameter and the imposed vertical strain, ε_{zz}, at the soil-shield gap (related to the increment in tunnel volume loss, $\Delta V_{L\ Sec.B}$) produce an increment in the surface volume loss ($\Delta V_{S\ Sec.B}$).

By the procedure reported in Appendix B, a specific point in the graphs of Figure 11 can be obtained, one for each case study. All the points seem well positioned along a line (the solid black line, hereafter called "correlation line"): the equations are reported also on the right of the graphs. In particular, Equations (6) and (7) represent respectively the "face" and "steady-state" conditions, by assuming a non-linear stiffness soil response (*HSs* model). Very high R^2 coefficients were found for both the correlations.

$$V_{S\ Sec.A} = 1.63\ V_{L\ Sec.A} + 0.01 \quad [\%] \tag{6}$$

$$\Delta V_{S\ Sec.\ B} = 1.12\ \Delta V_{L\ Sec.\ B} - 0.06 \quad [\%] \tag{7}$$

A close linear correlation was also observed between tunnel volume losses and imposed strains (ε_{yy} and ε_{zz}). The regression lines, Equation (8) and (9), are plotted as red lines in Figures 11a and 11b, for face and steady state conditions, respectively

$$\varepsilon_{yy} = -1.79\ V_{L\ Sec.A} \quad [\%] \tag{8}$$

$$\varepsilon_{zz} = -25.53\ \Delta V_{L\ Sec.B} + 2.91 \quad [\%] \tag{9}$$

Table 6 summarizes the values of the computed surface volume losses (V_S) and tunnel volume losses (V_L) for the five case histories, both at the face ($V_{Sec.A}$) and at the final steady-state condition (V_{tot}); the volume variations $\Delta V_{Sec.B}$ is also reported. The effects of dilatancy on the volume losses will be further investigated in Section 9. For coarse-grained soils, the surface volume loss can be lower or higher than the tunnel volume loss depending on the volumetric response of the soil mass, whether dilative or contractive behaviour prevails.

From the last column of the previous Table 6 it can be noted that the proportion between surface volume losses before the excavation face (Section A) and in steady-state conditions (Section B) it is not always

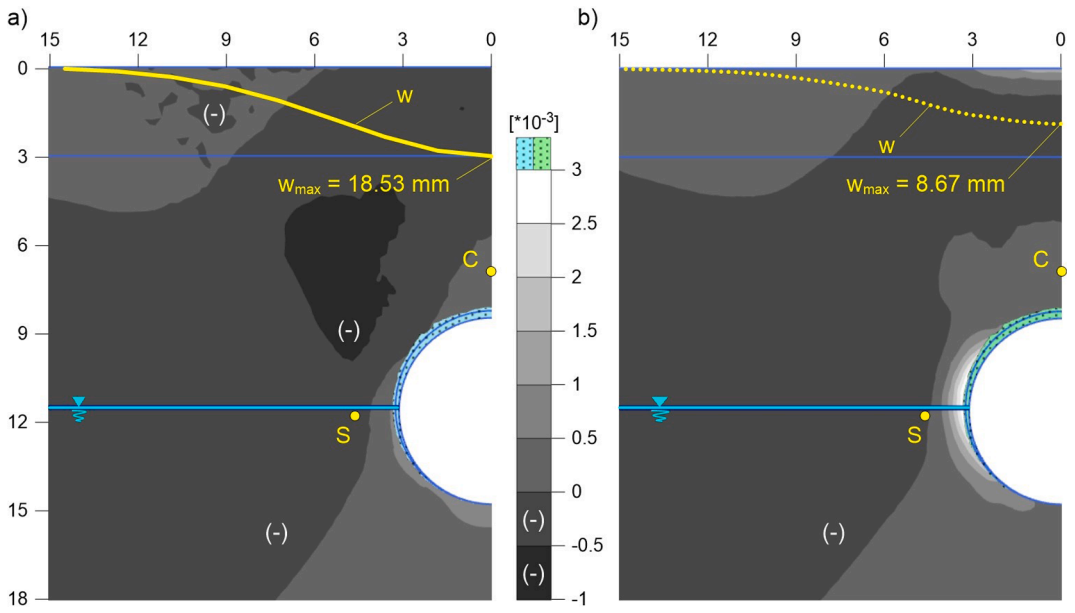

Fig. 19. Contours of the computed total volumetric strain (ε_v) at the steady-state: $\psi = 0°$ (a) and $\psi = 20°$ (b).

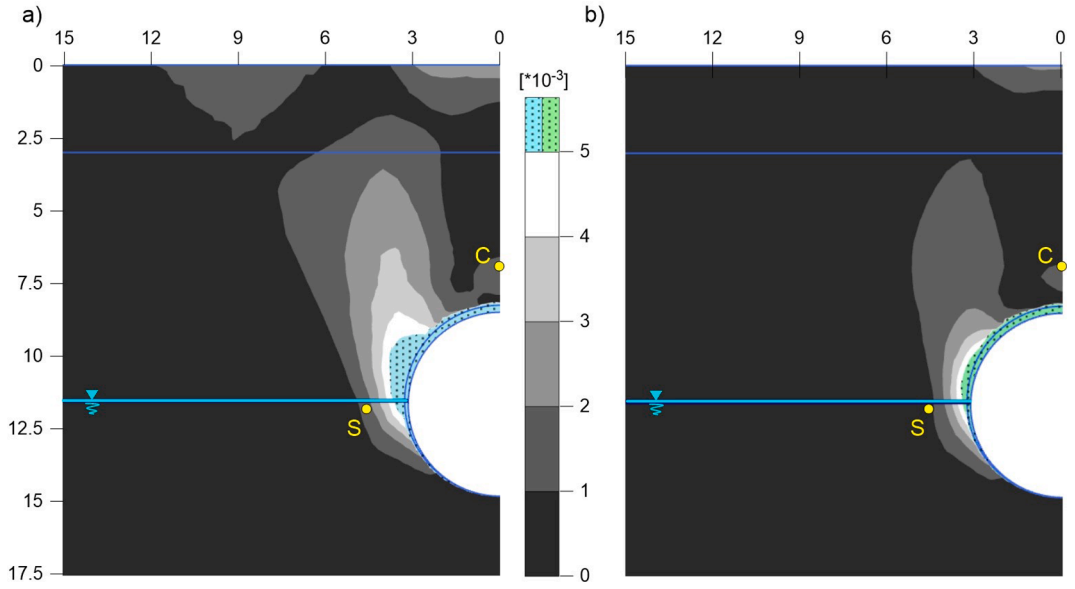

Fig. 20. Contours of the computed total deviatoric strain (γ_s) at the steady-state: $\psi = 0°$ (a) and $\psi = 20°$ (b).

constant but it varies in a quite wide range, from 17 % to 60 %. The mean value from this case selection can be calculated as 32 %, while it descends to 25.5 % if the Milan – M1 ext. case is excluded from calculation.

Farrell (2010) inferred that at low tunnel volume losses (V_L<1.0 %) there is little difference with V_S: this fact was particularly noticed in a series of centrifuge tests. A similar behaviour was observed for the case histories considered in this study (Table 6). In fact, the ratio between the final $V_{L\ tot}$ and $V_{S\ tot}$ is within the 1.00 – 1.23 interval.

8. Correlations as forecasting tool

The correlations obtained in the previous Section can be useful in the context of 2D modelling for tunnel design. In fact, Equations (6-9), which summarize the average response found in the five case histories, can be employed as a guideline to estimate model parameters for tunnels bored in similar conditions. To test the predictive capability of the aforementioned correlations, two further case histories of tunnels recently excavated in Italy were analyzed: the Brescia Metrobus (Sanzeni et al., 2010, Sanzeni et al., 2017) and the Milan M5 metro line (Fargnoli et al., 2013; Fargnoli et al., 2015). Both tunnels were excavated by EPB-shields in gravelly-sand soil deposits, with the water table approximately located at the elevation of the tunnel axis.

The soil profile and tunnel geometry of Brescia Metrobus and Milan – M5 are represented in Figure 12. In particular, field measurements and geotechnical parameters of the sections SCBF8 (Brescia Metrobus) and S942.2 (Milan – M5) were respectively considered. For additional details the reader is referred to the publications mentioned above.

Table 7 and Table 8 summarize the principal geometric data and soil parameters considered for each tunnel, Table 9 the mechanical parameters of the *HSs* soil model.

Figure 13 and Figure 14 show the surface settlements of the new case histories: measured data, respectively for Section A and Section B, are compared with model results and the empirical curves. The parameters

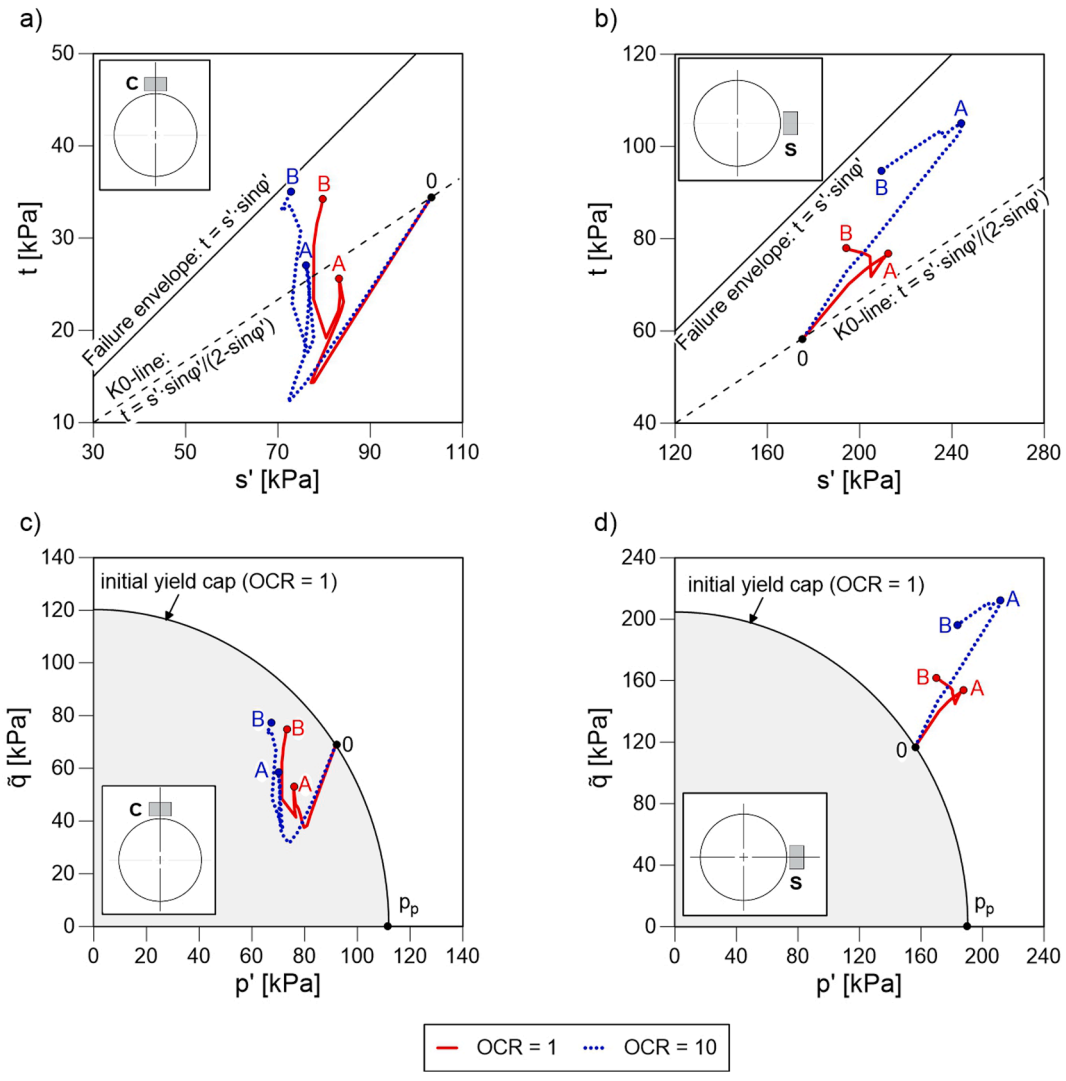

Fig. 21. Stress-paths in the *t-s'* plane at crown (a) and sidewall (b) and in the $\tilde{q}$-*p'* plane at crown (c) and sidewall (d) for different values of the over-consolidation ratio ($OCR = 1$, $OCR = 10$) for the Milan – M1 ext. tunnel.

of the empirical relationship were defined by data fitting, imposing that the curve passes through the maximum settlement point, $w_{Sec.B,}$ above the tunnel axis (Table 10). For the first case, Brescia Metrobus, upper and lower limits for the settlements at Section A (tunnel face section) were available from monitoring data, referred as day 3 and day 6, while the passage of the face through the section occurred approximately during day 4. The modelling results are in good agreement with field data, both in terms of shape of settlement trough and volume loss, and generally offer a better approximation than the empirical method. If the volume losses calculated for Brescia Metrobus and Milan – M5 are reported with the results of the 5 preceding cases, the new points are aligned with the correlation lines or very close to them (Figure 15). The correlation formulas of Equations (6-9) are therefore confirmed in their predictive potential.

Given the promising results, it is feasible to use the correlations of Equations –(6-9) to guide the modelling process for Class A predictions, i.e., for predictive analyses of the settlement trough performed at the design stage, before monitoring data are available. In fact, the strain parameters ε_{yy} and ε_{zz} required by the novel method can be immediately obtained from the "*Predictive lines*" of Equations (8-9), for a given "design value" of volume loss V_S, and consequently of V_L (Equations (6) and (7)). The "design value" of $V_{S\ tot}$ (the sum of $V_{S\ SecA}$ and $\Delta V_{S\ SecB}$) is typically intended to represent the maximum acceptable value, or an alarm value, which can be used to analyse and predict the effects induced by a new tunnelling project: generally, it is in the 0.5 – 1.0 % range (Lunardi et al., 2015; Franza et al., 2020).

An example of the possible use of Equations (6-9) as a forecasting tool is given in Figure 16, referring to the geotechnical conditions of the previously analysed Milan – M5 case.

In short, given a target total volume loss from design specification (e.g. $V_{S\ tot} = 0.5$ %), one should enter the two graphs in Figures 16a and 16b with a trail subdivision of $V_{S\ tot}$ in $V_{S\ Sec.A}$ and $\Delta V_{S\ Sec.B}$ (e.g. 25–75 %). Note that a $V_{S\ SecA}$ equal to the 25 % of $V_{S\ tot}$ represents to the mean value obtained for the 5 cases of Table 6. Following the arrows, the corresponding values of ε_{yy} and ε_{zz} with which to feed the FEM model can be derived. Thereafter, the computed $V_{S\ Sec.A}$ and $\Delta V_{S\ Sec.B}$ can be compared with the trial inputs: whether the two values are in good agreement or not, the process ends or a new trial subdivision is attempted until a satisfactory matching is found (Figures 16c and 16d). The next trial subdivision can be driven by the difference between the output and input $\Delta V_{S\ Sec.B}$ value of the previous iteration by applying the following relation:

$$(\Delta V_{S\ Sec.B})^{\ell+1}_{input} = (\Delta V_{S\ Sec.B})^{\ell}_{input} - \left[(\Delta V_{S\ Sec.B})^{\ell}_{output} - (\Delta V_{S\ Sec.B})^{\ell}_{input}\right] \quad [\%] \tag{10}$$

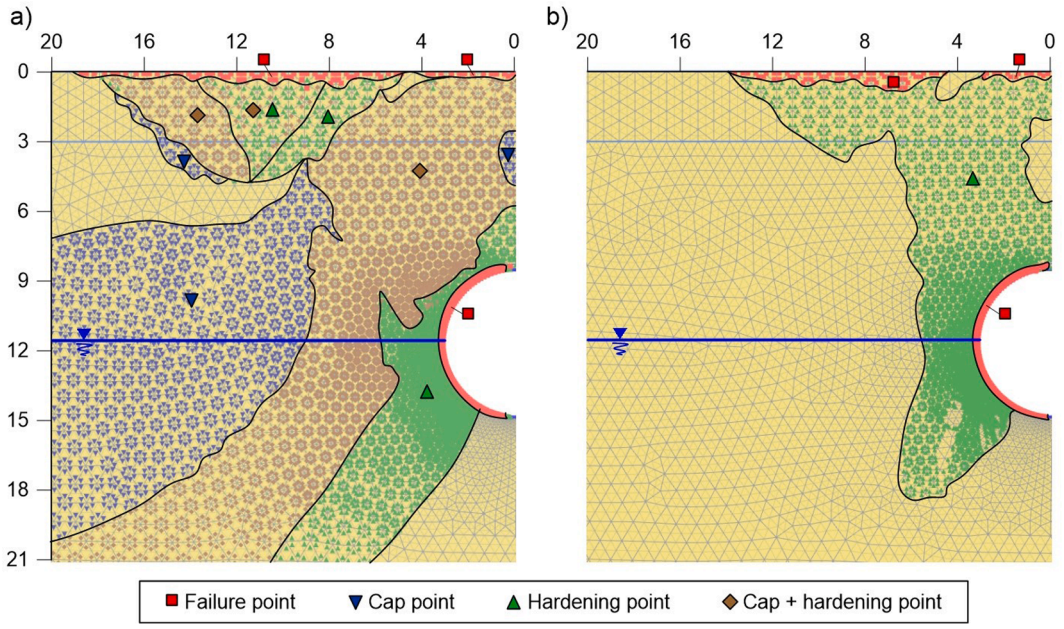

Fig. 22. Plastic stress points at the steady-state for $OCR = 1$ (a) and $OCR = 10$ (b).

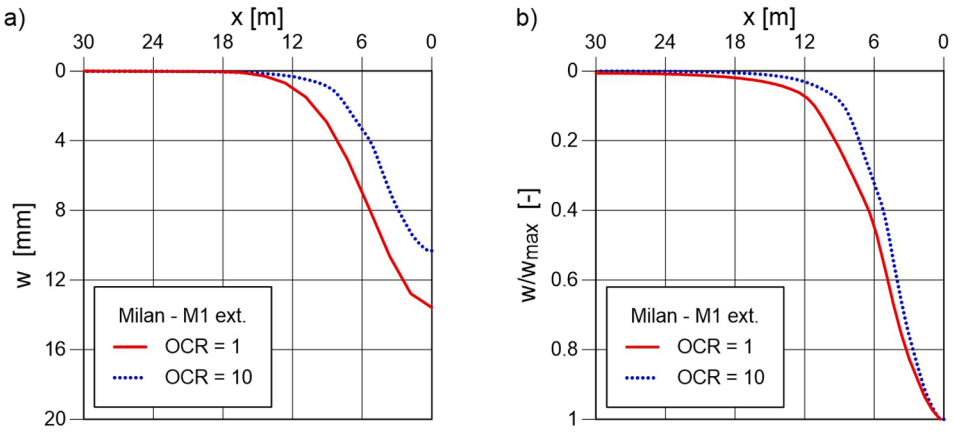

Fig. 23. Surface settlement troughs (a) and normalized surface settlement troughs (b) for $OCR = 1$ and $OCR = 10$.

where the superscript indicates the iteration number (ℓ) and the subscript distinguishes the trial *input* from the *output* of the FEM calculation. The portion of volume loss to be applied to the *Section A* phase is calculated according to $V_{S\ Sec.A} = V_{S\ tot} - \Delta V_{S\ Sec.B}$. In this example (Milan – M5 case), the ratio between $V_{S\ Sec.A}$ and $V_{S\ tot}$ at the end of the iterative procedure is around 57.5 %, very similar to the result of the Milan – M1 ext. case, reported in Table 6.

Fargnoli et al. (2013) analysed a monitoring section (S897.3) of Milan – M5, close to the previously analysed section (S942.2) and with similar geotechnical conditions. For this section, the monitoring data suggested a total volume loss of 0.48 %, very close to the input value of 0.5 % assumed in the calculation example. Figure 16e shows a nearly perfect matching between the trough predicted by FEM modelling and the monitoring data and, more in general, confirms the strength of the proposed approach.

9. Influence of dilatancy and volumetric cap

9.1. Dilatancy

In the *HSs* model the mobilized dilatancy angle can be calculated according to Rowe's theory (Rowe, 1962), at least for large values of mobilized friction, or by the approach proposed by Li and Dafalias (2000) when the Rowe's formula gives a negative angle.

For most of the preceding case histories, the dilatancy angle ψ was set equal to zero, in the absence of specific experimental determinations; only for the Milan – M1 ext. case a small value of $\psi = 10°$ was assumed. It is therefore worthwhile to analyze the influence of the dilatancy angle on the volume loss. To this aim, again the case of Milan – M1 ext. was selected, considering three different values of ψ (0, 10 and 20°).

The first observation concerns the surface settlement profiles: with increasing values of dilatancy the maximum settlement above the tunnel axis decreases (Figure 17a). However, the dilatancy effect does not change the shape of the settlement curves: in fact, in each case, the inflection point is approximately located at the same distance from the tunnel axis and the scaled settlement curves (Figure 17b), with respect to the specific w_{max}, are similar.

Figure 18 shows the calculated path of the total volume strain (ε_v) versus the deviatoric strain (γ_s) for two soil elements, located at a distance of only 1.5 m from the crown and the sidewall of the tunnel, therefore in zones markedly affected by the excavation effect and likely to experience large plastic strains. The initial stage (Phase 0) is located

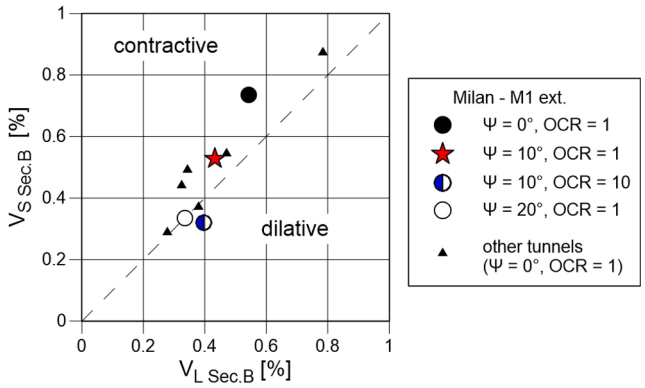

Fig. 24. Surface volume loss ($V_{S,Sec.B}$) related to the tunnel volume loss ($V_{L,Sec.B}$) for different angles of dilatancy ($\psi = 0°$, $\psi = 10°$, $\psi = 20°$) at the steady-state condition for tunnel Milan – M1 ext. in comparison with all the other cases.

at the origin and represents the undisturbed condition. The intermediate Phase corresponding to the face passage is labelled with the letter A, the final Phase with the letter B.

At the first calculation step, the soil element at crown expands (Figure 18, element C). The path is similar for the three cases up to the point A. After that (i.e., when vertical strains are applied to the soil-lining gap), the path separates into three branches: in case of null dilatancy the preceding expansion is almost recovered thanks to a contractive phase; with higher dilatancy angles the volumetric strain remains stable ($\psi = 10°$) or keeps increasing ($\psi = 20°$), reducing the maximum settlement above the tunnel axis. On the opposite, the sidewall element initially exhibits a contraction (Figure 18, element S), which is partially or almost completely recovered in the next phase, depending on the dilatancy angle.

For the same case study (Milan – M1 ext.), a potential calibration of the strain parameters under the hypothesis of $\psi = 0°$ would have led to lower values of ε_{yy} and ε_{zz} as observed for the for Naples – L6 case. In this respect, a careful assessment of relative density seems crucial for the coarse soil layer in which the tunnel is excavated.

Figure 19 shows the contours of the total volumetric strain ε_v for the two limit values of dilatancy ($\psi = 0°$ and 20°). Increasing ψ, the expansion strains (positive) at the sidewalls increase and positive volumetric strains also occur in a thin band of soil above the tunnel crown. When a non-dilative behaviour is assumed, expansion strains can be observed only in a small wedge of soil above the crown, other than below sidewalls and invert; the zone with more pronounced contraction strains is located above the springline at some distance from the tunnel wall. The deviatoric strain γ_s (Figure 20) are mainly concentrated in a wing-shaped zone of soil starting from the sidewalls, in both the considered cases. In the non-dilative case, the deviatoric strains are higher and the wing zone grows up towards the ground surface.

9.2. Volumetric cap

According to *HSs* model, the dilatancy angle is not the only parameter that may induce volume changes in the soil. In fact, irrecoverable volumetric strains may also be a consequence of compaction hardening under isotropic compression (see Appendix A), defined by means of a volumetric cap yield surface whose magnitude is a function of the isotropic preconsolidation stress, p_p. The initial value of p_p depends on the assigned over-consolidation ratio (*OCR*). Therefore, it is possible to inhibit the initiation of compaction hardening by fictitiously increasing the *OCR*.

A new analysis was therefore carried out purposely assuming $OCR = 10$, sufficient to completely inhibit the cap-yielding mechanism and, therefore, to appreciate its influence by comparison with the case $OCR = 1$. Figure 20 shows the stress-paths followed by two soil elements at a distance of 1.5 m from the crown and the sidewall, for $OCR = 1$ and 10. Moreover, the initial K_0 was always calculated with the Jaki formula, $1 - \sin\varphi'$, not dependent on *OCR*, to ensure that the initial stress state remains unchanged (same initial point O for the stress paths).

At the crown (Figure 21a), the first calculation stage (point A) determines a reduction in both mean, $s' = (\sigma_1' + \sigma_3')/2$, and deviator stress, $t = (\sigma_1' - \sigma_3')/2$. During the following stages (up to the final point B), while the mean stress s' remains almost constant, the deviator stress t increases; however, the *OCR* does not affect the stress-paths at crown significantly. On the contrary, the stress-paths at the sidewall (Figure 21b) for $OCR = 1$ and 10 differ remarkably: at the end of first stage, the increment in mean and deviator stress for $OCR = 1$ is only half of that observed for $OCR = 10$, owing to the reaching of the cap yield surface. In the following stages, the more relevant variation is the reduction in s'.

The stress paths of the same elements are also represented (Figures 21c and 21d) in the plane ($\tilde{q}, p'$), in which the cap yield function is defined, with $\tilde{q} = \sigma_1' + (\alpha\text{-}1)\,\sigma_2' - \alpha\sigma_3'$, $\alpha = (3 + \sin\varphi')/(3\text{-}\sin\varphi')$, and $p' = (\sigma_1' + \sigma_2' + \sigma_3')/3$. At the crown, the stress paths are similar and develop in the elastic domain. At the sidewall, while the stress path for $OCR = 1$, moving outwards of the initial yield cap, is influenced by the compaction hardening of the soil, the stress path for $OCR = 10$ develops within the very large boundaries of its elastic domain (not represented in Figure 21). It is worth noting that in this last case the initial state of stress does not lie on the initial yield cap, because the same K_0 value has been assumed, independently of the different *OCR*.

The effects of *OCR* on the stress state is also recognizable in Figure 22, in terms of plastic stress points. Red squares indicate that the stress lies on the failure surface, blue triangles represent a stress state that lies on the yield cap surface, brown diamonds lie on the shear and cap hardening envelope and green triangles lie on the shear-hardening envelope. When a large *OCR* is imposed ($OCR = 10$, Figure 22b) and the activation of the cap yield mechanism is excluded, the plastic strains are mainly concentrated around the tunnel, where the shear hardening activates and the failure condition is reached.

Reflecting the different distribution of plastic points, when the cap yield surface is deactivated, the ground surface settlements tend to reduce (Figure 23a) and the normalized curve becomes (Figure 23b) narrower (i.e., the inflection point is closer to the tunnel axis). The influence of the *OCR* is therefore different from that of the dilation angle, as it not only affects the magnitude, but also the shape of the settlement curve. A proper assessment of *OCR* is therefore particularly relevant for a correct prediction of the settlement trough.

9.3. Effect of plastic deformation on volume losses

It is now possible to thoroughly analyse the correlation between the surface volume loss V_S and the tunnel volume loss V_L at the steady state condition. To this aim, the total volume losses at the end of the analyses were considered, instead of analysing the partial effects at Section A and Section B. The final (V_L, V_S) points in Figure 24 show that the overall soil response remains contractive for a null or low dilatancy angle ($\psi = 0$, 10°), while it becomes substantially neutral when a larger dilatancy angle is considered ($\psi = 20°$). The deactivation of the compaction hardening ($OCR = 10$) causes a dilative behaviour in the soil, for a $\psi = 10°$. The foregoing sensitivity analysis was performed specifically for the case of the Milan – M1 ext. tunnel. For all the other tunnels considered in this paper, for which $\psi = 0°$ and $OCR = 1$, the final (V_L, V_S) points demonstrate that the overall response is generally contractive or, at the maximum, neutral.

This general trend is clearly observed in Figure 24, where the dashed line separates two portions of the graph: the upper area characterised by a contractive behaviour of the soil volume and the lower area where a dilative behaviour prevails. It is possible to infer that the contractive response generally prevails, also for a non-null value of dilatancy, due to the effect of the compaction hardening in the soil mass. This behaviour

should be carefully considered when a dense sand is found, or simply prevented by assuming a high *OCR* value, as shown in this Section.

10. Conclusions

The paper presents a specific approach, called the "*Strain applied method*", for FEM-2D modelling of soil-shield interaction in two calculation phases, useful for a simplified prediction of surface settlements caused by closed-face tunnelling. The overall volume loss at the tunnel boundary is obtained by applying volumetric strains to specific soil clusters. Two reference cross-sections of the tunnel can be analysed: the vertical plane passing through the tunnel face (Section A) and the steady-state conditions at distance from the face (Section B). The numerical analyses, carried out by the software Plaxis 2D, were performed with two soil models, the classic ideal elasto-plastic *Mohr-Coulomb* model and the *Hardening Soil with small strain stiffness* model, characterized by non-linear stiffness and two hardening mechanisms governing the shear and volumetric pre-failure deformation of the soil. The influence of dilatancy and compaction hardening on ground deformation were thoroughly analysed.

The study started with the calibration of the surface settlement trough predicted by the proposed approach, through the comparison with greenfield measurements, recorded in five well documented case histories of shallow tunnels bored in coarse-grained soil. The settlement troughs predicted by the *HSs* model are generally in better agreement with field observations and with the empirical Gaussian curve, both in terms of shape of the settlement trough and overall volume loss. Also the horizontal displacement distribution can be well predicted by this FEM approach, particularly at some distance from the tunnel axis, while some mismatch was found for displacements very close to the tunnel walls.

Specific correlations were determined between the ground volume loss at surface, *Vs*, the tunnel volume loss, V_L, and the strains, ε_{yy} and ε_{zz}, to be imposed at the tunnel boundary. By a comparative analysis of the selected case histories, it was possible to establish a set of trend lines, representative of the typical conditions for the current TBM tunnelling practice in coarse-grained deposits, which can be used as "*Predictive lines*" for tunnel excavated in similar conditions. Two further case histories of tunnelling in Italy were used as testing situations, to validate the reliability of the previously found correlations.

These "*Predictive lines*" take into account the combined effect of a large number of factors, such as: the typical features of TBM (slurry- and EPB- shields) and TBM operation (effective control of the face pressure, steering mode and muck conditioning parameters, for EPB shields), the generally accepted amount of ground loss for tunnelling in urban areas, the routinely sequence of lining installation and grouting. In fact, all the aforementioned features, although impossible to be explicitly included in a simple FEM − 2D model, may be relevant for the correct prediction of tunnelling effects in coarse-grained soils.

Out of the purposes of this paper, the "*Strain applied method*" was further validated by comparing it with other simplified methods for modelling the tunnel face advance in FEM − 2D analyses. In many cases, the new approach provided better outcomes in terms of surface displacements field. Moreover, the practical application of the "*Strain applied method*" can take advantage of the "*Predictive lines*" provided in this study. Being based on a set of case histories sharing specific features (range of depth, range of excavation diameters, typology of shield, soil type) the correlations found cannot be extended to tunnelling situations that substantially diverge from those analysed.

Moreover, the lack of monitoring data for the settlement trough near the tunnel face (i.e., during the transient excavation phase, before the final settlements are reached) did not allow a fully reliable comparison between measured and modelled results. In this regard, further refinements of the method are also possible: for instance, a non-isotropic deformation of the soil to be excavated in the first calculation phase (Section A, tunnel face cross-section) could be considered.

CRediT authorship contribution statement

F. Schiena: Writing – original draft, Formal analysis. **E. Lusini:** Writing – original draft, Visualization, Formal analysis, Methodology. **A. Lembo Fazio:** Supervision, Methodology, Conceptualization. **A. Graziani:** Writing – review & editing, Supervision, Methodology, Conceptualization.

Declaration of competing interest

The authors declare that they have no known competing financial interests or personal relationships that could have appeared to influence the work reported in this paper.

Data availability

data used in the paper are derived from published works

Acknowledgements

This research did not receive any specific grant from funding agencies in the public, commercial, or not-for-profit sectors.

A. Appendix

A.1. Essentials of the Hardening soil model with small strain stiffness (HSs)

The elasto-plastic with isotropic hardening *HSs* model (Benz, 2007) is an extension of the *Hardening Soil* model (Schanz et al., 1999). The model takes into account important features of soil behaviour, such as: high stiffness at small strain levels, development of plastic strains at first stages of loading and soil stiffness decrease with increasing strain level. *HSs* derives from the hyperbolic function based on the hyperbolic stress–strain relation proposed by Duncan and Chang (1963) in primary triaxial loading. The main parameters are:

- the resistance parameters c' (cohesion), φ' (friction angle), and ψ (dilatancy angle);
- the unloading/reloading Young's modulus, E_{ur}, the secant stiffness modulus, E_{50}, the oedometric tangent stiffness, E_{oed}.

The nonlinear isotropic elastic behaviour of the soil is considered by using a stress-dependent Young's modulus, which is a function of the effective stress and strength parameters according to the following expression:

$$E_{ur} = E_{ur}^{ref}\left(\frac{c'\cot\varphi' + \sigma'_3}{c'\cot\varphi' + p_{ref}}\right)^m \tag{A.1}$$

where E_{ur}^{ref} is the unloading/reloading Young's modulus at the reference pressure at 100 kPa ($p^{ref} = 100$ kPa). Soil behaviour is ruled by the stiffness

moduli listed above and depends on the minor principal stress σ'_3, which is the confining effective stress, and on the parameter m that controls the linear or non-linear response of the soil stiffness.

Similar relationships hold for the stress dependency of the secant stiffness modulus, E_{50}, and the tangent stiffness for primary oedometer loading, E_{oed}.

The *HSs* model considers two additional parameters, to those defined for the standard *HS* model, to take into account the dependency of soil stiffness on the strain level:

- the small-strain shear modulus, G_0;
- the shear strain, $\gamma_{0.7}$, at which the secant shear modulus is $G_s = 0.7\ G_0$.

The stress dependency of the small-strain shear modulus, G_0, is expressed by a relationship similar to the ones discussed above (Equation A.1) for the other stiffness.

$$G_0 = G_0^{ref}\left(\frac{c'\cot\varphi' + \sigma'_3}{c'\cot\varphi' + p_{ref}}\right)^m \tag{A.2}$$

The *HSs* model considers the modified version (Dos Santos and Correia, 2001) of the stiffness reduction curve proposed by Hardin and Drnevich (1972):

$$\frac{G_S}{G_0} = \frac{1}{1 + a\left|\frac{\gamma}{\gamma_{0.7}}\right|} \qquad a = 0.385 \tag{A.3}$$

The small-strain stiffness curve is cut off at the unloading/reloading shear modulus G_{ur}, defined as:

$$G_{ur} = \frac{E_{ur}}{2(1+\upsilon_{ur})} \tag{A.4}$$

where υ_{ur} is the Poisson's ratio for unloading/reloading.

The *HSs* model comprises two yield surfaces, not fixed in the principal stress space but which can evolve following a hardening rule. A shear hardening yield surface, f^s, which is a function of the plastic strains due to the primary deviatoric loading and a cap yield surface, f^c, which depends on the plastic volumetric strain due to primary compression. The flow rule is associated for states lying on the surface f^c, whereas a non-associated flow rule is adopted for states on the surface f^s, by adopting a formulation based on stress-dilatancy theory.

The shear yield (f^s) loci can expand up to the ultimate *Mohr-Coulomb* failure surface, while the cap surface (f^c) can expand as a function of the pre-consolidation stress, p_p, which, in turn, depends on the initial *OCR* value. Schanz et al. (1999) give the complete description of the model.

B. Appendix

B.1. Volume loss calculation procedure

The deformed volume of soil clusters is internally calculated by the software Plaxis 2D. However, the built-in procedure is not available for the deactivated soil clusters (e.g., the excavated volume) or the clusters with small volume and distorted elements (e.g., the lunette-shaped volume in Figure 4).

The first issue was overcome by applying the 'shoelace' formula to the initial and deformed nodal coordinates of the plate, which represents the final lining. The formula (Equation B.1) approximates the shape of the excavation profile with a polygon, connecting the N adjacent nodes, and calculates the nominal volume, $V_{excavated,n}$, from nodes coordinates (x_j,y_j) and the deformed volume $V_{excavated,f}$, from the coordinates updated with displacements ($x_j + u_x$, $y_j + u_y$). This formula introduce an approximation in the calculated volume, but the error is negligible when considering the volume variation of Equation (B.2), if the number of nodes (N) is reasonably high.

$$2\,V_{excavated} = \begin{vmatrix} x_1 & x_2 & \cdots & x_j & \cdots & x_N \\ y_1 & y_2 & \ldots & y_j & \ldots & y_N \end{vmatrix} \tag{B.1}$$

$$\Delta V_{excavated} = V_{excavated,f} - V_{excavated,n} \tag{B.2}$$

where $\Delta V_{excavated}$ is the volume loss, $j = 1\ldots N$ is the number of the nodes of the plate representing the lining.

The volumetric deformation of the soil clusters was calculated by a Matlab script by the same method utilized in Plaxis 2D (Brinkgreve et al., 2017). For each cluster the volume loss (or gain) is calculated as follow:

$$\Delta V_{cluster} = \frac{1}{2}\sum_{i=1}^{M}\left(\sum_{ii=1}^{3} W_{ii}\det\left(\begin{bmatrix} \frac{\partial N}{\partial \xi}(\xi_{ii},\eta_{ii}) \\ \frac{\partial N}{\partial \eta}(\xi_{ii},\eta_{ii}) \end{bmatrix}\begin{bmatrix} X_{el} & Y_{el} \end{bmatrix}\right)\right) \tag{B.3}$$

where $i = 1\ldots M$ is the number of elements in each cluster, $ii = 1\ldots 3$ is the element Gauss point, W_{ii} is the weight of the Gauss point, $\boldsymbol{N}$(1x6) is the vector of element shape functions, (ξ, η) are the coordinates of the six-node triangular element in the parent domain, $\boldsymbol{X}_{el}$(6x1) and $\boldsymbol{Y}_{el}$(6x1) are the vectors of

element nodes in global coordinates.

The surface volume loss, V_S, is calculated by Equation (B.4), while Equation (B.5) is used for obtaining the tunnel volume loss, V_L

$$V_S = 100\left(\frac{\sum_{k\in\Omega}\Delta V_k + \Delta V_{excavated}}{\frac{\pi D_f^2}{4}}\right)[\%] \tag{B.4}$$

$$V_L = 100\left(\frac{\sum_{k\in\Pi}\Delta V_k + \Delta V_{excavated}}{\frac{\pi D_f^2}{4}}\right)[\%] \tag{B.5}$$

where k are the (active) soil clusters, Ω is the set of all active soil clusters and Π is the set of soil clusters to which the prescribed strain (ε_{yy} or ε_{zz}) is applied.

References

Addenbrooke, T.I., Potts, D.M., Puzrin, A.M., 1997. The influence of pre-failure soil stiffness on the numerical analysis of tunnel construction. Géotechnique 47 (3), 693–712.

Attewell, P.B., Yeates, J., Selby, A.R., 1986. Soil movements induced by tunnelling and their effects on pipelines and structures. Blackie, Glasgow.

Attewell, P.B., Woodman, J.P., 1982. Predicting the dynamics of ground settlement and its derivatives caused by tunnelling in soil. Ground Eng. 15 (8), 13–22.

Bakker, K.J., de Boer, F., Admiraal, J.B.M., van Jaarsveld, E.P., 1999. Monitoring pilot projects using bored tunnelling: the Second Heinenoord Tunnel and the Botlek Rail Tunnel. Tunn. Undergr. Space Technol. 14 (2), 121–129.

Benz, T., 2007. Doctoral thesis: Small-strain stiffness of soils and its numerical consequences. Institute of Geotechnical Engineering, University of Stuttgart.

Bilotta, E., Paolillo, A., Russo, G., Aversa, S., 2017. Displacements induced by tunnelling under a historical building. Tunn. Undergr. Space Technol. 61, 221–232.

Bilotta, E., Russo, G., 2012. Ground movements induced by tunnel boring in Naples. In: Viggiani, C. (Ed.), Geotechnical Aspects of Underground Construction in Soft Ground. Taylor & Francis Group, London, pp. 979–986.

Boldini, D., Spaggiari, C., Abul, J.K., Fuoco, S., Lusini, E., 2023. Class A predictions of damage level in an historical fortress induced by twin tunnelling, in: Expanding underground - Knowledge and passion to make a positive impact on the world: Proceedings of the ITA-AITES World Tunnel Congress 2023 (WTC 2023), 12-18 May 2023, Athens, Greece. CRC Press, London, pp. 1788-1795.

Boldini, D., Losacco, N., Franza, A., DeJong, M.J., Xu, J., Marshall, A.M., 2021. Tunneling-induced deformation of bare frame structures on sand: numerical study of building deformations. J. Geotech. Geoenviron. Eng. 147 (11).

Boscardin, M.D., Cording, E.J., 1989. Building response to excavation-induced settlements. J. Geotech. Eng. 115(1), 1-21.

Breth, H., Chambosse, G., 1975. Settlement behavior of buildingsabove subway tunnels in Frankfurt clay. In: Settlement of Structures: Conference Organised by the British Geotechnical Society at the Lady Mitchell Hall, Cambridge Held in April 1974. Pentech Press, London, pp. 329–336.

Brinkgreve, R.B.J., Engin, E., Swolfs, W.M., 2017. Plaxis 2D Manual. Balkema, Rotterdam.

Burd, H.J., Houlsby, G.T., Augarde, C.E., Liu, G., 2000. Modelling tunnelling-induced settlement of masonry buildings. Proc. Inst. Civ. Eng. Geotech. Eng. 143 (1), 17–29.

Celentano, P., Bilotta, E., Russo, G., Aversa, S., 2017. Effetti dello scavo di una galleria urbana su un edificio intelaiato, in: Moraci, N., Soccodato, C. (Eds.), La Geotecnica nella conservazione e tutela del patrimonio costruito: XXVI Convegno Nazionale di Geotecnica - Roma 2017. AGI, pp. 527-534.

Celestino, T.B., Gomes, R.A.M.P., Bortolucci, A.A., 2000. Errors in ground distortions due to settlement trough adjustment. Tunn. Undergr. Space Technol. 15 (1), 97–100.

DAUB (Deutscher Ausschussfür Unterirdisches Bauen), 2021. Recommendations for the Selection of Tunnel Boring Machines.

Dos Santos, J.A., Correia, A.G., 2001. Reference threshold shear strain of soil. Its application to obtain an unique strain-dependent shear modulus curve for soil, in: Proceedings of the Fifteenth International Conference on Soil Mechanics and Geotechnical Engineering, Istanbul, 27-31 August 2001. Balkema, Rotterdam, pp. 267-270.

Duhme, R., Lee, J., 2021. Latest Developments in Shield TBM Selections & Design for Mechanized Tunneling. in: Proc. of the 2021 World Congress on Advances in Structural Engineering and Mechanics, Seoul, 24-26 August 2021.

Duncan, J.M., Chang, C.Y., 1963. Nonlinear analysis of stress and strain in soil. J. Soil Mech. Found. Div. 96 (5), 1629–1653.

El-Nahhas, F.M., El-Mossallamy, Y.M., 2009. The role of small strain constitutive model for predicting differential settlement above tunnels, in: Proc. of the 13th Int. Conf. on Structural and Geotechnical Engineering, Cairo, 27-29 December 2009.

El-Nahhas, F.M., El-Mossallamy, Y.M., El-Shamy, A.A., 2015. 3D analysis of ground settlement induced by machanized tunnelling, in: Proc. of the 14th Int. Conf. on Structural and Geotechnical Engineering, Cairo, 20-22 December 2015.

Fargnoli, V., Boldini, D., Amorosi, A., 2013. TBM tunnelling-induced settlements in coarse-grained soils: the case of the new Milan underground line 5. Tunn. Undergr. Space Technol. 38, 336–347.

Fargnoli, V., Boldini, D., Amorosi, A., 2015. Twin tunnel excavation in coarse grained soils: observations and numerical back-predictions under free field conditions and in presence of a surface structure. Tunn. Undergr. Space Technol. 49, 454–469.

Farrell, R.P., 2010. Doctoral thesis: Tunnelling in sands and the response of building. HYPERLINK "http://www.eng.cam.ac.uk/" Department of Engineering, University of Cambridge.

Franza, A., Marshall, A.M., Zhou, B., 2019. Greenfield tunnelling in sands: the effects of soil density and relative depth. Géotechnique 69 (4), 297–307.

Franza, A., Marshall, A.M., Zhou, B., Shirlaw, N., Boone, S., 2020. Greenfield tunnelling in sands: the effects of soil density and relative depth (Discussion). Géotechnique 70 (7), 639–646.

Hardin, B.O., Drnevich, V.P., 1972. Shear modulus and damping in soils: design equations and curves. J. Soil Mech. Found. Div. 98 (7), 667–692.

Hejazi, Y., Dias, D., Kastner, R., 2008. Impact of constitutive models on the numerical analysis of underground constructions. Acta Geotech. 3, 251–258.

ITA/AITES (International Tunnelling Association), 2000. Recommendations and Guidelines for Tunnel Boring Machines – Working Group N.14 (Mechanized Tunnelling).

Kavvadas, M., Litsas, D., Vazaios, I., Fortsakis, P., 2017. Development of a 3D finite element model for shield EPB tunnelling. Tunn. Undergr. Space Technol. 65, 22–34.

Lambrughi, A., Medina Rodriguez, L., Castellanza, R., 2012. Development and validation of a 3D numerical model for TBM–EPB mechanised excavations. Computers Ang Geotechnics 40, 97–113.

Lee, K.M., Rowe, R.K., Lo, K.Y., 1992. Subsidence owing to tunnelling. I. Estimating the gap parameter. Can. Geotech. J. 29, 929–940.

Li, X.S., Dafalias, Y.F., 2000. Dilatancy for Cohesionless Soils. Géotechnique 50 (4), 449–460.

Lunardi, G., Mancinelli, L., Zimbaldi, A., Carini, M., 2015. Copenhagen Cityringen Metro: EPB-TBM head pressure definition, in. Proceedings of ITA-AITES World Tunnel Congress 2015 (WTC 2015)/41st General Assembly.

Mair, R.J., Taylor, R.N., 1997. Theme lecture: Bored tunnelling in the urban environment, in: Proceedings of the fourteenth international conference on soil mechanics and foundation engineering, Hamburg, 6-12 September, 1997. Balkema, Rotterdam, pp. 2353-2385.

Mair, R.J., 2003. Research on tunnelling-induced ground movements and their effects on buildings – lessons from the Jubilee Line Extension, in: Jardine, F.M. (Ed.), Response of buildings to excavation-induced ground movements: Proceedings of the international conference held at Imperial College, London, UK on 17-18 July 2001. CIRIA, pp. 3-26.

Marshall, A.M., Farrell, R., Klar, A., Mair, R., 2012. Tunnels in sands: the effect of size, depth and volume loss on greenfield displacements. Géotechnique 62 (5), 385–399.

Migliazza, M., Chiorboli, M., Giani, G.P., 2009. Comparison of analytical method, 3D finite element model with experimental subsidence measurements resulting from the extension of the Milan underground. Comput. Geotech. 36, 113–124.

Möller, S.C., Vermeer, P.A., 2008. On numerical simulation of tunnel installation. Tunn. Undergr. Space Technol. 23 (4), 461–475.

Möller, S.C., 2006. Doctoral thesis: Tunnel induced settlements and structural forces in linings. Institute of Geotechnical Engineering, University of Stuttgart.

Ochmański, M., Modoni, G., Bzówka, J., 2018. Automated numerical modelling for the control of EPB technology. Tunn. Undergr. Space Technol. 75, 117–128.

O'Reilly, M.P., New, B.M., 1982. Settlements above tunnels in the United Kindom – Their magnitudes and prediction. in: Jones, M.J. (Ed.), HYPERLINK "https://search.worldcat.org/it/title/889517498" Tunnelling '82: papers presented at the third international symposium . Institution of Mining and Metallurgy, London, pp. 173-181.

Panet, M., Guenot, A., 1983. Analysis of convergence behind the face of a tunnel. In: Tunnelling 82, proceedings of the 3rd international symposium, Brighton, 7–11 June 1982, pp. 197–204.

Peck, R.B., 1969. Deep excavations and tunneling in soft ground, in: Proceedings of the Seventh International Conference on Soil Mechanics Foundation Engineering. Sociedad Mexicana de Mecánica de Suelos, Mexico City, pp. 225-290.

Pelizza, S., 2002. La scelta del metodo di scavo meccanizzato integrale in ambiente urbano. in: XXI Convegno Nazionale di Geotecnica, L'Aquila: Opere geotecniche in ambiente urbano. Pàtron, pp. 50-66.

Rowe, P.W., 1962. The stress-dilatancy relation for static equilibrium of an assembly of particles in contact. Proceedings of the Royal Society of London – Series A, Mathematical and Physical Sciences 269(1339), 500-527.

Rowe, R.K., Lo, K.Y., Kack, G.J., 1983. A method of estimating surface settlement above tunnels constructed in soft ground. Canadian Geotechnical Journal 20 (1), 11–22.

Sanzeni, A., Giuriani, E., Colleselli, F., 2017. Il consolidamento delle fondazioni del palazzo della loggia di Brescia. in: Moraci, N., Soccodato, C. (Eds.), La Geotecnica nella conservazione e tutela del patrimonio costruito: XXVI Convegno Nazionale di Geotecnica - Roma 2017. AGI, pp. 745-752.

Sanzeni, A., Zinelli, L., Colleselli, F., 2010. Estimated settlements during the Brescia Metrobus tunnel excavation. In: Benz, T., Nordal, S. (Eds.), Numerical Methods in Geotechnical Engineering. CRC Press, London, pp. 789–794.

Schanz, T., Vermeer, P.A., Bonnier, P.G., 1999. Formulation and verification of the Hardening-Soil Model. In: Brinkgreve, R.B.J. (Ed.), Beyond 2000 in Computational Geotechnics. Balkema, Rotterdam, pp. 281–290.

Schiena, F., 2020. Doctoral thesis: Predicting effects induced by shallow mechanized tunnelling in coarse-grained soils. Department of Engineering, "Roma Tre" University.

Song, G., Marshall, A.M., 2020. Centrifuge modelling of tunnelling induced ground displacements: pressure and displacement control tunnels. Tunn. Undergr. Space Technol. 103 (103461).

Van Jaarsveld, E.P., Plekkenpol, J.W., van de Graaf, C.A., 1999. Ground deformations due to the boring of the Second Heinenoord tunnel. In: Barends, F.B.J., Lindenberg, J., Luger, H.J., de Quelerij, L., Verruijt, A. (Eds.), Geotechnical Engineering for Transportation Infrastructure: Theory and Practice, Planning and Design. Balkema, Rotterdam, pp. 153–160.

Vermeer, P.A., Brinkgreve, R., 1993. PLAXIS Version 5 Manual. Balkema, Rotterdam.

Viggiani, G.M.B., Standing, J.R., 2001. The Treasury. In: Burland, J.B., Standing, J.R., Jardine, F.M. (Eds.), Building Response to Tunnelling: Case Studies from Construction of the Jubilee Line Extension. London, Thomas Telford, London, pp. 401–432.

Vorster, T.E.B., Klar, A., Soga, K., Mair, R.J., 2005. Estimating the effects of tunneling on existing pipelines. J. Geotech. Geoenviron. Eng. 131 (11), 1399–1410.

Xu, J., Franza, A., Marshall, A.M., Losacco, N., 2021. Role of Footing Embedment on Tunnel-Foundation Interaction. J. Geotech. Geoenviron. Eng. 147 (9).